

附件 2 浙江水利水电学院“南浔青年学者”申请表

姓 名	马瑞芳	出生年月年龄 (年龄)	1987 年 12 月岁 (34 岁)	参加工作时间	2019 年 7 月
现所在单位 (部门)	浙江水利水电学院	最高学历/学位	研究生/博士	专业技术职务	专任教师
符合条款	符合科研类，科研论文，发表 3 类期刊论文 2 篇，总绩点 100。				
所涉业绩	教学类 绩点: <u>1</u>				
	科研类 绩点: <u>100</u>	Offset Initial Sodium Loss To Improve Coulombic Efficiency and Stability of Sodium Dual-Ion Batteries. Ruifang Ma, Ling Fan, Suhua Chen, Zengxi Wei, Yuhua Yang, Hongguan Yang, Yong Qin, Bingan Lu. ACS Appl. Mater. Interfaces. 2018, 10 (18), 15751-15759. (3 类期刊论文) (SCI TOP 中科院一区)			
		Confined and covalent sulfur for stable room temperature potassium-sulfur battery. Ruifang Ma, Ling Fan, Jue Wang, Bingan Lu. Electrochimica Acta. 2019, 293, 191-198. (3 类期刊论文) (SCI TOP 中科院二区)			
	人才称号类 绩点: <u>1</u>				
	总绩点	100			
个人承诺	本人承诺上述所填内容真实、准确；如有不实，本人承担相应责任。 签名: <u>马瑞芳</u> 时间: <u>2022.11.25</u>				
以上部分由申请人填写，所在单位审核。以下由单位（部门）和学校填写。					
所在单位 (部门) 意见	1.经审核，申请人所填内容： <input type="checkbox"/> 属实 <input type="checkbox"/> 不属实； 2.是否符合所申请的类别： <input type="checkbox"/> 符合 <input type="checkbox"/> 不符合； 3.是否同意推荐： <input type="checkbox"/> 同意 <input type="checkbox"/> 不同意。 负责人签名：_____ (部门盖章) _____年____月____日				
科技处 审核意见	负责人签名：_____ (部门盖章) _____年____月____日	教务处 审核意见	负责人签名：_____ (部门盖章) _____年____月____日		
其他相关职能 部门审核意见	负责人签名：_____ (部门盖章) _____年____月____日				
学校意见	(学校盖章) _____年____月____日				

经检索《Web of Science》和《Journal Citation Reports (JCR)》数据库,《Science Citation Index Expanded (SCI-EXPANDED)》收录论文及其期刊影响因子如下。(检索时间: 2022年11月25日)

第1条, 共2条

标题:Offset Initial Sodium Loss To Improve Coulombic Efficiency and Stability of Sodium Dual-Ion Batteries

作者:Ma, RF(Ma, Ruifang);Fan, L(Fan, Ling);Chen, SH(Chen, Suhua);Wei, ZX(Wei, Zengxi);Yang, YH(Yang, Yuhua);Yang, HG(Yang, Hongguan);Qin, Y(Qin, Yong);Lu, BA(Lu, Bingan);

来源出版物:ACS APPLIED MATERIALS & INTERFACES 卷:10 期:18

页:15751-15759DOI:10.1021/acsami.8b03648 出版年:MAY 9 2018

影响因子:10.383 (2021)

入藏号:WOS:000432205800048

语种:English

文献类型:Article

地址:

[Ma, Ruifang; Fan, Ling; Chen, Suhua; Wei, Zengxi; Yang, Yuhua; Yang, Hongguan; Lu, Bingan] Hunan Univ, State Key Lab Adv Design & Mfg Vehicle Body, Sch Phys & Elect, Changsha 410082, Hunan, Peoples R China.

[Lu, Bingan] Mat Technol Co Ltd, Wing Lok St, Sheung Wan 999077, Hong Kong, Peoples R China.

[Qin, Yong; Lu, Bingan] Chinese Acad Sci, Inst Coal Chem, State Key Lab Coal Convers, Taiyuan 030001, Shanxi, Peoples R China.

通讯作者地址:

Fan, L; Lu, BA (corresponding author), Hunan Univ, State Key Lab Adv Design & Mfg Vehicle Body, Sch Phys & Elect, Changsha 410082, Hunan, Peoples R China.; Lu, BA (corresponding author), Mat Technol Co Ltd, Wing Lok St, Sheung Wan 999077, Hong Kong, Peoples R China.; Qin, Y; Lu, BA (corresponding author), Chinese Acad Sci, Inst Coal Chem, State Key Lab Coal Convers, Taiyuan 030001, Shanxi, Peoples R China.

电子邮件地址:fanling@hnu.edu.cn; qinyong@siccc.ac.cn; luba2012@hnu.edu.cn

IDS号:GF8FX

ISSN:1944-8244

eISSN:

来源出版物页码计数:9

第2条, 共2条

标题:Confined and covalent sulfur for stable room temperature potassium-sulfur battery

作者:Ma, RF(Ma, Ruifang);Fan, L(Fan, Ling);Wang, J(Wang, Jue);Lu, BG(Lu, Bingan);

来源出版物:ELECTROCHIMICA ACTA 卷:293 页:191-198DOI:10.1016/j.electacta.2018.10.040 出版年:JAN 10 2019

影响因子:7.336 (2021)

入藏号:WOS:000451333900021

语种:English

文献类型:Article

地址:

[Ma, Ruifang; Fan, Ling; Wang, Jue; Lu, Bingan] Hunan Univ, Sch Phys & Elect, Changsha 410082, Hunan, Peoples R China.

[Lu, Bingan] Chinese Acad Sci, Inst Coal Chem, State Key Lab Coal Convers, Xian 030001, Shaanxi, Peoples R China.

[Wang, Jue] Mat Technol Co Ltd, Wing Lok St, Sheung Wan 999077, Hong Kong, Peoples R China.

[Lu, Bingan] Fujian Strait Res Inst Ind Graphene Technol, Jinjang 362200, Peoples R China.

通讯作者地址:

Lu, BG (corresponding author), Hunan Univ, Sch Phys & Elect, Changsha 410082, Hunan, Peoples R China.

电子邮件地址:luba2012@hnu.edu.cn

IDS 号:HB8JF

ISSN:0013-4686

eISSN:1873-3859

来源出版物页码计数:8

注:

期刊影响因子为当前最新版。

他引次数—论文被非论文作者引用次数。

以上检索结果均得到被检索人的确认。



Offset Initial Sodium Loss To Improve Coulombic Efficiency and Stability of Sodium Dual-Ion Batteries

Ruifang Ma,^{†,||} Ling Fan,^{*,†,||} Suhua Chen,[†] Zengxi Wei,[†] Yuhua Yang,[†] Hongguan Yang,[†] Yong Qin,^{*,§} and Bingan Lu^{*,†,‡,§}

[†]School of Physics and Electronics, State Key Laboratory of Advanced Design and Manufacturing for Vehicle Body, Hunan University, Changsha 410082, China

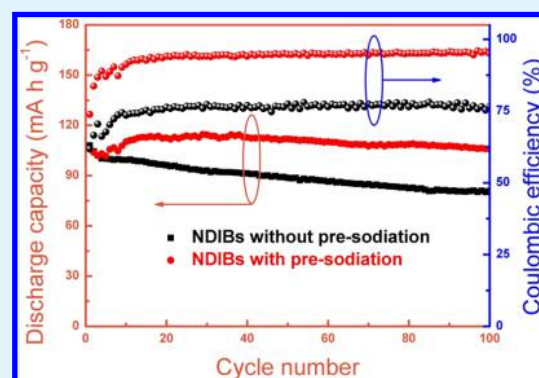
[‡]Material Technology Company Limited, Wing Lok Street, Sheung Wan, Hong Kong 999077, China

[§]State Key Laboratory of Coal Conversion, Institute of Coal Chemistry, Chinese Academy of Sciences, Taiyuan 030001, Shanxi, China

S Supporting Information

ABSTRACT: Sodium dual-ion batteries (NDIBs) are attracting extensive attention recently because of their low cost and abundant sodium resources. However, the low capacity of the carbonaceous anode would reduce the energy density, and the formation of the solid-electrolyte interphase (SEI) in the anode during the initial cycles will lead to large amount consumption of Na⁺ in the electrolyte, which results in low Coulombic efficiency and inferior stability of the NDIBs. To address these issues, a phosphorus-doped soft carbon (P-SC) anode combined with a presodiation process is developed to enhance the performance of the NDIBs. The phosphorus atom doping could enhance the electric conductivity and further improve the sodium storage property. On the other hand, an SEI could preform in the anode during the presodiation process; thus the anode has no need to consume large amounts of Na⁺ to form the SEI during the cycling of the NDIBs. Consequently, the NDIBs with P-SC anode after the presodiation process exhibit high Coulombic efficiency (over 90%) and long cycle stability (81 mA h g⁻¹ at 1000 mA g⁻¹ after 900 cycles with capacity retention of 81.8%), far more superior to the unsodiated NDIBs. This work may provide guidance for developing high performance NDIBs in the future.

KEYWORDS: sodium dual ion battery, anodes, pre-sodiation, phosphorus-doped soft carbon



1. INTRODUCTION

Rechargeable batteries, which could promote the shift from petrol (gasoline)-powered vehicles to electrically powered vehicles, have attracted extensive attention for decades.¹ However, the further application of traditional lithium-ion batteries for large-scale electric energy storage systems (EESs) is hindered by the high cost and limited lithium resources.² Therefore, more and more researchers are working on alternative rechargeable batteries, such as sodium-ion batteries (SIBs),^{3–11} potassium-ion batteries,^{12–14} metal–sulfur batteries,^{15–18} and dual-ion batteries (DIBs).^{19–31} Among the various rechargeable batteries, DIBs are considered to be the effective, low cost, and eco-friendly EESs for energy storage.^{22,24,27,32} As we know, the energy density of the whole battery could be improved by improving the voltage of the cathode or lowering the voltage of the anode. Therefore, it is important to develop advanced cathode/anode materials to meet the need of the high-energy SIBs.^{33–36} It is known that the anions could insert/desert into/from graphite cathodes at high voltage in DIBs, which could improve the voltage of the full cell, further leading to enhanced energy density. Moreover,

the abundant and low cost graphite resources will further reduce the cost of the batteries. In addition, these merits have made the graphite a promising cathode for DIBs. In contrast to the traditional rocking-chair batteries, cations together with anions are contributing to the specific capacities of DIBs during charge/discharge processes.³⁷ Typically, the anions/cations in the electrolyte intercalate into cathode/anode materials during the charge process and deintercalate from cathode/anode back to the electrolyte during the discharge process.³⁸ In the past, extensive investigation of electrolytes in DIBs focused on lithium-based salts and other ionic liquids.^{25,37,39–41} Until recently, the sodium-based DIBs (NDIBs) have been developed and attracted much attention because of the abundance and low cost of sodium resources.^{24,42}

It is known that the anodes of SIBs usually suffer from a large amount of sodium loss because of the solid-electrolyte interphase (SEI) formation during the initial cycle, and the

Received: March 4, 2018

Accepted: April 17, 2018

Published: April 17, 2018

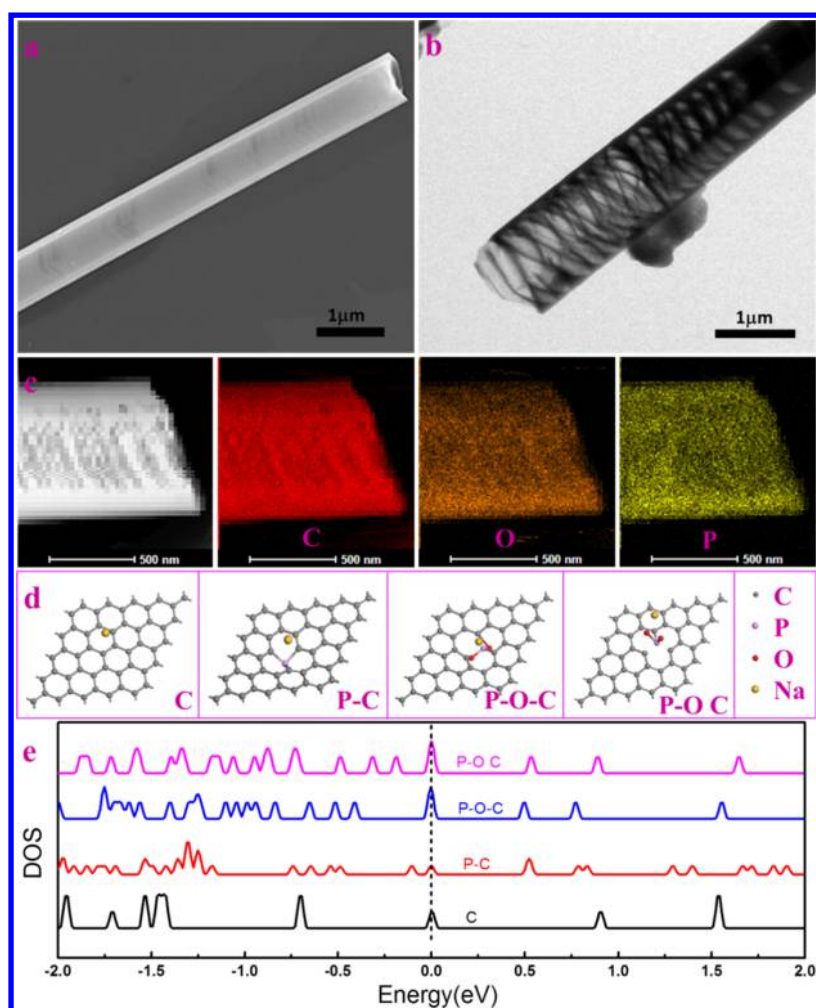


Figure 1. The morphology of the P-SC. (a) SEM, (b) TEM, (c) EDS elemental mapping of P-SC, and (d) geometric structures for Na adsorption on the C and the P-SC (including P-C, P-O-C and P-O C) monolayer of top views. (e) Density of states (DOS) for the C and the P-SC (including P-C, P-O-C, and P-O C).

initial Coulombic efficiency (ICE) of SIBs mostly is lower than 70%.^{33,43–46} In the sodium half cells, the influence of this trouble is unobvious because of the far in excess of sodium in the sodium electrode. As this problem will result in severe issues in the full cells, including low capacity, inferior cycle stability, and limited lifespan, it should be treated with caution. The NDIBs suffer from, not surprisingly, low Coulombic efficiency and inferior cycle stability as well.^{22,24,27,37} In addition, the low capacity of carbonaceous anode and the sodium depletion in the electrolyte would significantly reduce the capacity and energy density of NDIBs. Therefore, it is urgent to develop new anode materials with high capacity and new methods to offset the initial irreversible loss of sodium ions.^{47,48}

In this contribution, we synthesized a high capacity phosphorus-doped soft carbon (P-SC) anode and demonstrated a valid approach to offset the initial sodium loss via anode presodiation. As a consequence, the NDIBs with the P-SC anode after presodiation exhibited improved Coulombic efficiency (>90%), high discharge capacity (118 mA h g⁻¹ at 500 mA g⁻¹), excellent rate performance, and long cycle stability (81 mA h g⁻¹ after 900 cycles at 1000 mA g⁻¹ with capacity retention of 81.8%), much superior to the unsodiated NDIBs (u-NDIBs), which delivers poor Coulombic efficiency

of 75% and inferior cycle stability (44 mA h g⁻¹ after 400 cycles at 1000 mA g⁻¹ with a capacity retention of 47.8%).

2. EXPERIMENTAL SECTION

Pyrolysis of perylene tetracarboxylic dianhydride (PTCDA) as a feasible method to obtain soft carbon (SC) has been reported.^{42,49,50} PTCDA was purchased from J&K Scientific, and used as received. The P-SC and SC were obtained from thermal polymerization of PTCDA with a slow heating rate. Typically, in order to obtain the P-SC, 2 g PTCDA and 2 g phosphorus powder were homogeneously mixed and placed into a quartz boat and then annealed at 600 °C under Ar atmosphere for 4 h with a heating rate of 2 °C min⁻¹. For the synthesis of SC, 2 g pure PTCDA was annealed at 600 °C under Ar atmosphere for 4 h with a heating rate of 2 °C min⁻¹.

2.1. Material Characterizations. The microstructure morphology of P-SC and SC was studied via FE-SEM (Hitachi S-4800) equipped with an X-ray energy-dispersive spectrometer and JEOL JEM-2100F TEM. X-ray diffraction (XRD; Philips, X'Pert Pro) was conducted using Cu K α radiation ($\lambda = 0.154056$ nm) over a 2θ range of 5°–80° to investigate the crystalline structure of P-SC and SC. Raman spectra of P-SC and SC were measured via a Renishaw 2000 system. X-ray photoelectron spectroscopy (XPS) analysis of P-SC and SC was conducted via ESCALAB 250Xi. BET surface area measurements were performed with a Quantachrome instrument (Quabrasorb SI-3MP). Electronic conductivity measurements were carried out at room temperature using the four-point method. The sample disk for the measurement was compacted through a hydraulic system.

2.2. Calculations Method. The first principle was carried out with the Cambridge Sequential Total Energy Package, and in which projected-augmented-wave potential was performed. Moreover, the Perdew–Burke–Ernzerhof and generalized gradient approximation were carried out in the electronic exchange–correlation energy calculations. In all the calculations, the results were performed to be converged, in which the maximum stress was lower than 0.01 GPa, the maximum force on the atom was lower than $0.01 \text{ kcal mol}^{-1} \text{ \AA}^{-1}$, and the maximum displacement was below $1 \times 10^{-5} \text{ \AA}$.

2.3. Electrochemical Measurements. The P-SC or SC/ acetylene black/carboxyl methylated cellulose (7:2:1, w/w/w) was dissolved into the solution of $\text{C}_2\text{H}_5\text{OH}/\text{H}_2\text{O}$ (1:2.5, w/w) and stirred for 8 h. The mixture was pasted onto a thin copper foil and then dried at $65 \text{ }^\circ\text{C}$ in a vacuum oven. The weight of the active material was about $0.8\text{--}1.2 \text{ mg cm}^{-2}$. The graphite cathode was prepared with a weight ratio of graphite/acetylene black/carboxyl methylated cellulose (8:1:1, w/w/w) and cased onto an aluminum foil. Sodium-ion half cells (SIBs) were assembled with 2032-type coin cell in a glovebox under Ar ($\text{H}_2\text{O} < 0.5 \text{ ppm}$, $\text{O}_2 < 0.5 \text{ ppm}$) using sodium metal as the counter electrode. The sodium-based dual-ion full cells (NDIBs) were assembled with graphite as the cathode; the weight ratio of graphite/P-SC in NDIBs is around 3:1, which is the optimized cathode/anode capacity ratio. The electrolyte used for NDIBs was 1 M NaPF_6 in EC/DMC (6:4, v/v). The separator membrane used for both SIBs and NDIBs was Whatman G/A. The amount of the electrolyte for each cell was around $60 \text{ }\mu\text{L}$ for SIBs and $120 \text{ }\mu\text{L}$ for NDIBs. The galvanostatic charge/discharge process was investigated via Arbin Instrument BT 2000 model. For SIBs, the charge/discharge voltage range was $3.0\text{--}0.01 \text{ V}$ (vs Na^+/Na). Cyclic voltammetry (CV) curves were performed in the electrochemical workstation at a scan rate of 0.1 mV s^{-1} with a voltage range from 3.0 to 0.01 V (vs Na^+/Na). For the NDIBs and the graphite cathode in the SIB, the galvanostatic charge/discharge processes were all investigated with the voltage range of $2.0\text{--}4.7 \text{ V}$. All the capacities were calculated from the weight of the anode materials. The anode presodiation process was as the following. The P-SC was assembled for SIBs and cycled for one cycle to allow the formation of SEI in the anode, and then, the P-SC electrode was taken out from the SIBs and assembled for NDIBs for the subsequent measurements.

3. RESULTS AND DISCUSSIONS

It is reported that SC synthesized at a high temperature of $900 \text{ }^\circ\text{C}$ exhibits high ICE around 80% for SIBs recently, and when the SC was used as an anode for NDIBs, the battery could deliver excellent cycle stability and Coulombic efficiency.⁴² Therefore, in order to acquire high capacity anode with low ICE (<70%) for sodium storage, SC and P-SC were facilely synthesized at a relative low temperature of $600 \text{ }^\circ\text{C}$. Scanning electron microscopy (SEM) and transmission electron microscopy (TEM) were conducted to investigate the morphology of the as prepared P-SC and SC. The SEM image of P-SC (Figure S1a) clearly revealed that the structure of P-SC was composed of many microrods, with the diameter of a single microrod about $1 \text{ }\mu\text{m}$. It was clear that the surface of the single microrod was quite smooth, which was confirmed via the SEM and TEM images in Figure 1a,b. Furthermore, the transversal striations were observed in both SEM and TEM images (Figure S1b,c), which could be interpreted as the oriented crystallite growth of perylene-3,4,9,10-tetracarboxylic dianhydride (PTCDA) during the pyrolysis process.⁵¹ High-resolution TEM (HRTEM) was performed to investigate some selected micro area of the P-SC. As shown in Figure S1d, lattice fringes with a specific orientation were observed, consistent with the oriented crystallite growth of PTCDA, indicating the existence of the localized microcrystalline structure in P-SC. In order to investigate the element distribution of P-SC, energy-dispersive spectroscopy (EDS) elemental mapping (Figure 1c)

was performed. The EDS elemental mapping showed the uniform distribution of carbon, oxygen, and phosphorus, indicating that the phosphorus atoms had been homogeneously doped into the carbonaceous substrate. The atomic contents of C, O and P were 93.68, 5.22 and 1.09%, respectively.

As a comparison, the SEM image of SC (Figure S2a) revealed that the SC also had a microrod structure with a diameter of a single microrod about $3\text{--}5 \text{ }\mu\text{m}$, which was much bigger than that of P-SC. The transversal striations could also be observed in SEM (Figure S2b) and TEM images (Figure S2c). In addition, unobvious lattice fringes were observed in the HRTEM image (Figure S2d), indicating the disordered structure of SC. The different morphologies between P-SC and SC (as observed from the SEM and TEM images) were probably because of the phosphorus doping in P-SC. For the nature of the sp^2 -bond of carbon, the electron-rich P-SC lattices could easily lead to “out of plane” bonding configurations, which may induce curvature and closure of the system during growth. Hence, the microrod size of P-SC became smaller.⁵²

To further characterize P-SC and SC, XRD and XPS measurements were performed. The XRD patterns (Figure S3a) of P-SC and SC exhibit two major humpy peaks at around 24.8° and 43.2° , corresponding to the (002) and (100) planes of SC, respectively.⁵² Moreover, XPS measurements were carried out to further investigate the chemical structures of P-SC and SC. Figure S3b shows the full survey XPS of P-SC. Five peaks at around 18, 135, 192, 285, and 533 eV were assigned to the O 2s, P 2p, C 1s, and O 2s, respectively. In addition, the amount of C, O, and P in P-SC calculated via XPS was 93.15, 5.77, and 1.08% by atomic content, respectively, close to the values determined by EDS. The high-resolution P 2p XPS spectrum of P-SC in Figure S3c showed two main peaks at 134.2 and 135.0 eV, corresponding to the bond of P–O and P–C, respectively.⁵³ The XPS results indicated that the phosphorus atoms had been successfully and uniformly incorporated into the P-SC. In contrast, the full survey XPS curve of SC (Figure S3d) revealed only three peaks at 18, 285, and 533 eV, attributed to O 2s, C 1s, and O 1s, respectively. The amount of C and O in SC was 98.36 and 1.64% by the atomic content, respectively. Besides, Raman spectra (Figure S3e) were used to evaluate the degree of structural formation of P-SC and SC. There are two distinct peaks located at around 1340 and 1485 cm^{-1} , corresponding to the D band and G band, respectively. Generally, the intensity ratio (I_D/I_G) of D band and G band could be used for gauge for the amount of structure defects.⁵⁴ It is obvious that the I_D/I_G increased from 0.971 for SC to 1.098 for P-SC, and this phenomenon might be due to the increased content of phosphorus and oxygen functional groups in P-SC encouraging it to be more disordered. In addition, the increased functional groups in P-SC are beneficial for the electrode to obtain high capacity.

To evaluate the total specific surface area (SSA) of P-SC and SC, nitrogen adsorption/desorption isotherms measurements were conducted. As shown in Figure S4a, the SSA of P-SC was only $1.15 \text{ m}^2 \text{ g}^{-1}$, with the pore diameters (Figure S4b) of P-SC around $5\text{--}14 \text{ nm}$. As a comparison, the SSA of SC is $9.81 \text{ m}^2 \text{ g}^{-1}$, with the pore diameters around $20\text{--}60 \text{ nm}$ (Figure S4c,d). The low surface area of P-SC and SC indicated the close packing of P-SC and SC, which was beneficial for obtaining high volumetric energy density.

In order to explore the effect of the phosphorus doping, density functional theory (DFT) calculations were implemented with pristine carbon and different phosphorus-doped

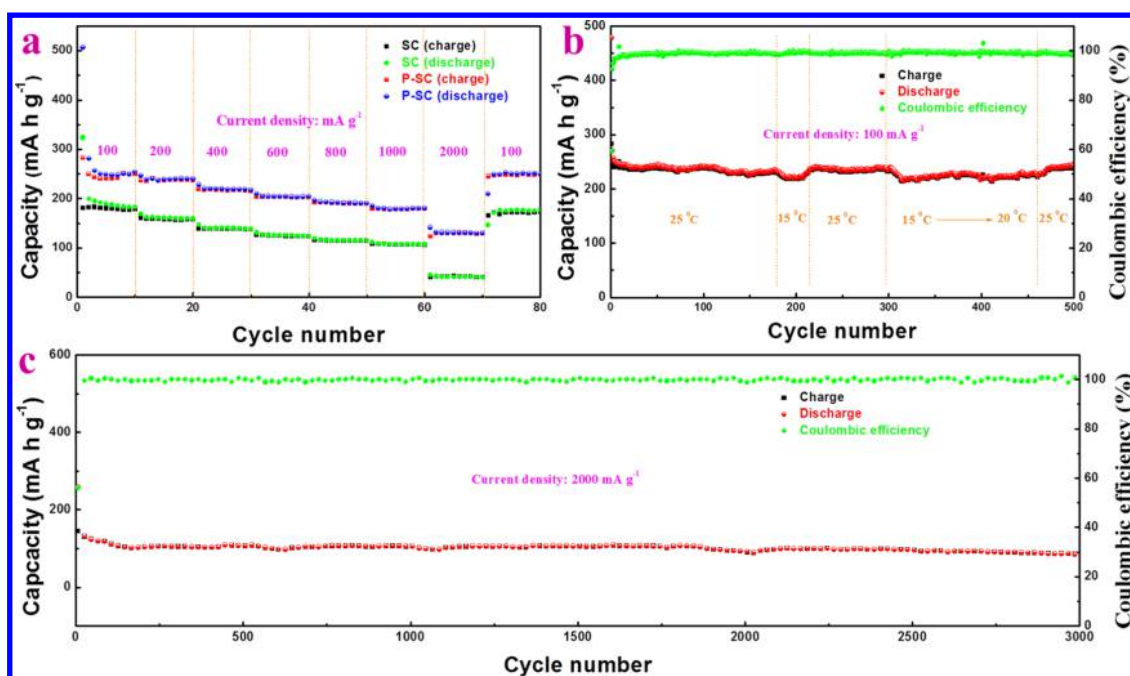


Figure 2. (a) The rate performance of P-SC and SC at current densities from 100 to 2000 mA g⁻¹. The long cycling of P-SC at a current density of (b) 100 and (c) 2000 mA g⁻¹.

carbon chemical structures (Figure 1d). The bonding between atoms was analyzed from electronic density states. It could be found that the DOS of the SC (named as C) and P-SC with possible structures (including C–P, P–O–C, and P–O–C) (Figure 1e) elucidates that both the SC and P-SC were metallic, which is similar to the reported results.^{52,53} Besides, remarkable new peaks nearby the Fermi energy level in the conduction band were brought by the incorporation of phosphorus and oxygen atoms into the carbon and forming bonds of C–P, C–P–O–C, or C–P–O. In other words, the phosphorus atom or phosphorus–oxygen bonds incorporated into SC would improve the metallic behavior and interrupt the polarized transport degeneracy of the SC, resulting in a transformation of SC from the intrinsic semiconductor to n-type semiconductor, which is conducive to the fast sodium storage performance.^{53,54} We also performed the electronic conductivity of P-SC and SC to meet the DOS result. The electronic conductivity of P-SC was 9.79×10^{-3} S/cm, which was an order of magnitude larger than that of SC (7.46×10^{-4} S/cm). Finally, the peaks at the Fermi energy of sodium overlapped with other elements for P-SC with C–P and C–P–O–C bonds (Figure S5b,c), indicating interaction between them, while, no peaks at the Fermi energy of sodium for SC and P-SC with C–P–O bonds appeared (Figure S5a,d). Furthermore, the Na-adsorption energies of P-SC with C–P were more negative than that of SC, which was consistent with the recent findings.⁵⁵ Above all, the DFT calculation further indicated that the phosphorus-doping could enhance the sodium storage properties.

In order to investigate the Na⁺ storage capacity of P-SC and SC, half cells were assembled in a glovebox using sodium metal as the counter electrode. CV curves were performed to investigate the Na⁺ storage mechanism of P-SC and SC. As shown in Figure S6a, the CV curves of P-SC exhibited a broad peak at 1.0–0.3 V in the initial discharge process, which disappeared in the subsequent cycles. The broad peak was believed to be mainly due to the formation of the SEI.⁵⁰ Nonetheless, in the subsequent discharge cycles, a sloping

region located at 0.25–1.0 V was observed, which was attributed to the Na⁺ reacted with the functional groups in the P-SC. In addition, the cathode peak at around 0.01 V was mainly due to the Na⁺ insert into the SC.⁵⁶ During the charge processes, only a humpy peak located at 0.1–1.0 V was observed, which could be interpreted as the deintercalation of Na⁺ from the SC and the functional groups. As a comparison, the discharge processes of SC (Figure S6b) only revealed one peak at around 0.01 V. This could be due to the lack of P atoms in the SC, leading to less functional group. In addition, this reason could be used to explain the disappearance of the humpy sloping region of 0.5–1.0 V during discharge of SC when compared with P-SC.

Different electrochemical properties between P-SC and SC could be further confirmed via the charge/discharge profiles (Figure S7a). According to the initial discharge/charge curves of P-SC and SC, the discharge/charge capacity of P-SC and SC were 478/283 mA h g⁻¹ and 323/180 mA h g⁻¹, corresponding to an ICE of 59.2 and 55.7%, respectively. Again, the large irreversible sodium loss during the initial cycle was attributed to the formation of the SEI. Besides, the discharge profiles of P-SC and SC could be divided into two regions. The high voltage region of P-SC and SC at 1.0–0.25 V could be interpreted as the Na⁺ reacted with the functional groups in the carbonaceous substrate and the low voltage platform below 0.25 V was due to the insertion of Na⁺ into the SC. It was clear that the discharge capacity of P-SC (312 mA h g⁻¹) was higher than that of SC (196 mA h g⁻¹) at the high voltage region (over 0.25 V vs Na⁺/Na), which again could be accounted for more functional groups of P-SC than that of SC. The superior electrochemical property of P-SC could be further demonstrated by rate performance (Figure 2a). Apparently, P-SC showed higher capacity at various current densities than that of SC. The P-SC (vs SC) delivered a capacity of 256 (vs 195), 245 (vs 162), 220 (vs 140), 204 (vs 126), 193 (vs 115), 180 (vs 108), and 131 (vs 41) mA h g⁻¹ at various current densities of 100, 200, 400, 600, 800, 1000, and 2000 mA g⁻¹, respectively. The corresponding

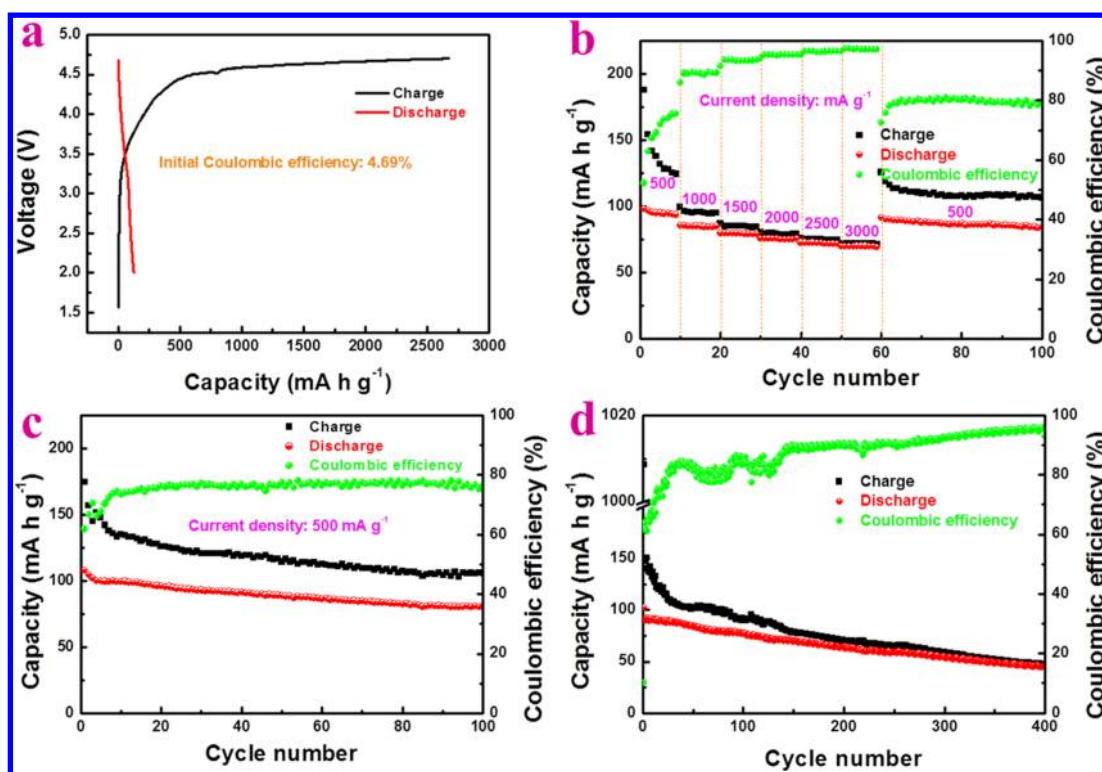


Figure 3. Electrochemical performance of the NDIBs with the configuration of unsodiated P-SC (anode)|1 M NaPF₆ (electrolyte)|graphite (cathode), named u-NDIBs. (a) Initial charge/discharge profile of the u-NDIBs at the current density of 500 mA g⁻¹. (b) Rate property of the u-NDIBs at various current densities from 500 to 3000 mA g⁻¹ from the second cycles. (c) Cycling stability of the u-NDIBs at the current density of 500 mA g⁻¹ from the second cycles. (d) Cycling stability of the u-NDIBs at the current density of 1000 mA g⁻¹.

discharge/charge curves of P-SC and SC at various current densities are shown in Figure S8a,b, respectively. Notably, when the current density returned back to 100 mA g⁻¹ after 80 cycles at various current densities, the P-SC (vs SC) could still recover a reversible capacity of 252 (vs 171) mA h g⁻¹, indicating the excellent rate recyclability of both P-SC and SC.

In addition to the outstanding rate performance, P-SC also exhibited preeminent long cycle stability (Figure 2b,c). Figure 2b shows the cycle stability of P-SC at a current density of 100 mA g⁻¹. A reversible capacity of 242 mA h g⁻¹ was obtained even after 500 times of repeated discharge/charge processes (with capacity retention of 89.7% or capacity decay of 0.0206% per cycle, based on the capacity of the second discharge). It was worth mentioning that when the environment temperature decreased to 15 °C, a capacity of 220 mA h g⁻¹ could still be retained (91.6% capacity maintained with respect to the capacity at 25 °C) at 100 mA g⁻¹. When the environment temperature rose back to 25 °C, the capacity still could recover to 240 mA h g⁻¹. For convenience, the discharge/charge curves of P-SC at different cycles and different temperatures are shown in Figure S9. There was no obvious difference in the charge/discharge platform of P-SC after 500 cycles, indicating the superior cyclability of P-SC. Furthermore, the cycle stability of SC (Figure S7b) and P-SC (Figure 2c) was further investigated at a high current density of 2000 mA g⁻¹. Notably, a reversible capacity of 89 mA h g⁻¹ of P-SC still retained even after 3000 cycles, with capacity retention of 68.5% (or capacity decay of 0.010% per cycle) based on the capacity of the second discharge. However, the capacity of SC is relatively low and decayed rapidly. The comparison of the P-SC anode with other carbonaceous anodes reported in previously literatures are presented in Table S1.

Besides, the rod structure of the P-SC was maintained even after sequential discharge/charge processes. Figure S10a–c shows the SEM, TEM, and HRTEM images of the P-SC after 500 cycles at the current density of 100 mA g⁻¹, respectively. It was obvious that the similar rod structure is still retained. As the rod shape morphology could provide the stable framework and electron transportation channels, which was responsible for the superior long cycle stability.⁵² On the other hand, the phosphorus doping could significantly reduce the impendence of the SIBs (agrees well with the DFT calculations), which was crucial for the P-SC to achieve superior electrochemical properties (Figure S11).

In view of the superior rate performance and low ICE (59.2%) of the P-SC, the sodium-based dual-ion full batteries (NDIBs) were assembled to investigate the importance of offset the initial sodium loss in NDIBs. The typical charge/discharge profile of graphite cathode in Na half-cells is presented in Figure S12a. The NDIBs were assembled with the configuration of unsodiated P-SC (anode)|NaPF₆ (electrolyte)|graphite (cathode), named u-NDIBs. It could be seen that the u-NDIBs delivers an initial charge/discharge capacity of 2673/125 mA g⁻¹, corresponding to an ICE of 4.69% (Figure 3a). The extremely low ICE of the u-NDIBs was possibly caused by the large amount of sodium loss in the initial cycle (due to the formation of SEI in the anode) and was detrimental for any practical applications. The rate performance of the u-NDIBs (Figure 3b) showed discharge capacity of 95, 85, 79, 75, 72, and 69 mA h g⁻¹ at the current density of 500, 1000, 1500, 2000, 2500, and 3000 mA g⁻¹, respectively. In addition, the corresponding charge/discharge profiles of the u-NDIBs at various current densities are shown in Figure S12b. Furthermore, the cycling of the u-NDIBs (Figure 3c) exhibited

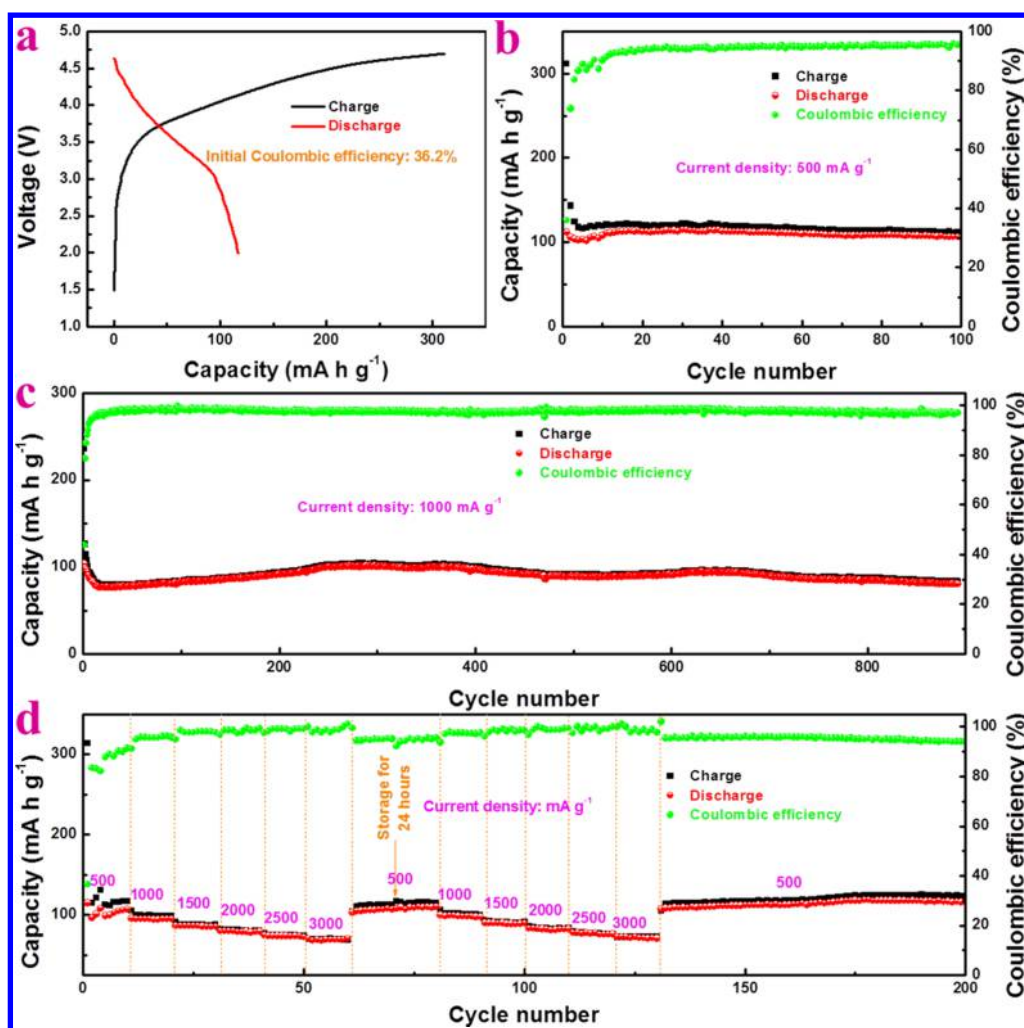


Figure 4. The electrochemical performance of the NDIBs with the configuration of presodiated P-SC (anode)|1 M NaPF₆ (electrolyte)|graphite (cathode), named p-NDIBs. (a) The initial charge/discharge profile of the p-NDIBs at the current density of 500 mA g⁻¹. (b) The cycling stability of the p-NDIBs at the current density of 500 mA g⁻¹. (c) The cycling stability of the p-NDIBs at the current density of 1000 mA g⁻¹. (d) The rate property of the p-NDIBs at various current densities from 500 to 3000 mA g⁻¹.

a reversible capacity of 79 mA h g⁻¹ after 100 cycles with a capacity retention of 73.1% based on the second discharge. However, the Coulombic efficiency of the u-NDIBs at 500 mA g⁻¹ is below 80%. Moreover, when the current density increased to 1000 mA g⁻¹ (Figure 3d), a poor cycling stability was obtained with a reversible capacity of 44 mA h g⁻¹ after 400 cycles, with a capacity retention of only 47.8% based on the second discharge. The large amount SEI formation in the anode during the initial charge process can be the one utmost reason for the inferior electrochemical properties of the u-NDIBs, further resulting in a poor Coulombic efficiency and inferior cycling stability of the u-NDIBs.

To resolve the above problem, we proposed an anode presodiation method prior to assembling the NDIBs. The detailed anode presodiation process was as the following: the P-SC anode was assembled into SIBs first and was cycled only once to allow the formation of the SEI in the P-SC; then, the P-SC electrode was taken out from the SIBs and assembled the NDIBs for the subsequent measurements, named p-NDIBs. The initial charge/discharge profile of the p-NDIBs (Figure 4a) exhibited a charge/discharge capacity of 309/112 mA h g⁻¹, corresponding to an ICE of 36.2%, which was around 8 times higher than that of u-NDIBs. The typical CV curve at a scan

rate of 0.5 mV s⁻¹ is shown in Figure S13a. Moreover, the cycle stability of the NDIBs after presodiation was also improved significantly. It could deliver a reversible capacity over 110 mA h g⁻¹ after 100 cycles without obvious capacity decay (Figure 4b). The Coulombic efficiency increased to 95% after a few cycles, much higher than that of u-NDIBs (beneath 80%). Furthermore, when a high current density of 1000 mA g⁻¹ was applied (Figure 4c), a reversible capacity of 81 mA h g⁻¹ was obtained after 900 cycles with capacity retention of 81.8%, corresponding to a capacity decay of 0.02% per cycle. It was worth mentioning that the Coulombic efficiency was up to 98%, except for the initial several cycles.

The p-NDIBs not only presented excellent cycle stability and high Coulombic efficiency but also exhibited superior rate performance. The p-NDIBs delivered a discharge capacity of 108, 98, 89, 83, 78, and 73 mA h g⁻¹ at the current density of 500, 1000, 1500, 2000, 2500, and 3000 mA g⁻¹, respectively (Figure 4d). Furthermore, when the p-NDIBs was stored for 24 h after various cycles, it still delivered excellent cycling stability and rate performance, with a reversible capacity of 118 mA h g⁻¹ at 500 mA g⁻¹ even after 200 cycles at various current densities. In particular, the p-NDIBs exhibited Coulombic efficiency over 90% after several cycles, which was much higher

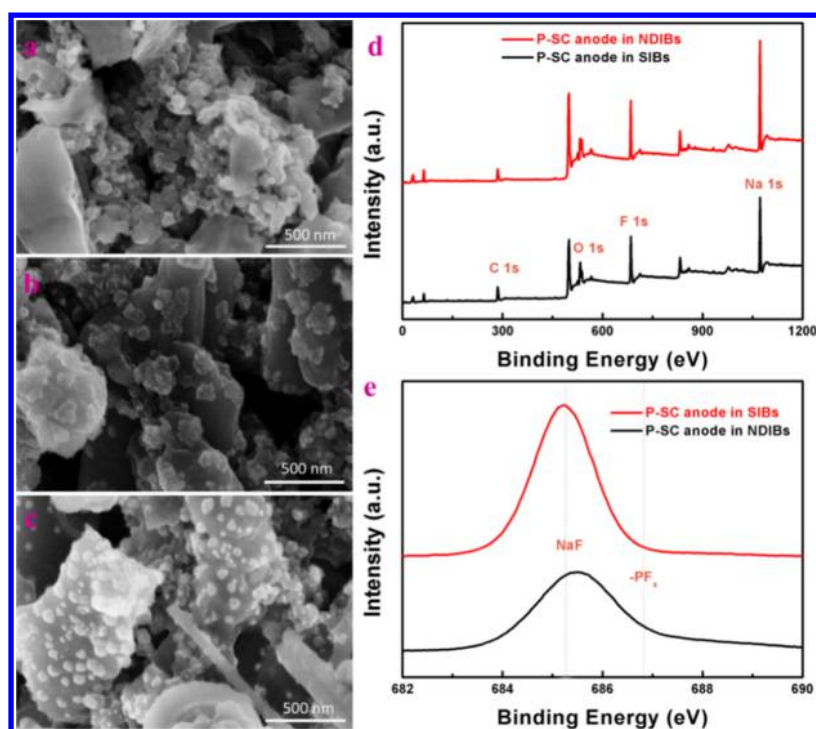


Figure 5. The SEM image of the P-SC electrode at the state of (a) pristine, (b) after anode presodiation, and (c) after the initial cycle of the NDIBs without anode presodiation. (d) The full XPS survey and (e) high-resolution F 1s XPS of the P-SC electrode. The SEM and XPS have proved the SEI formation during the initial cycles for both NDIBs and SIBs.

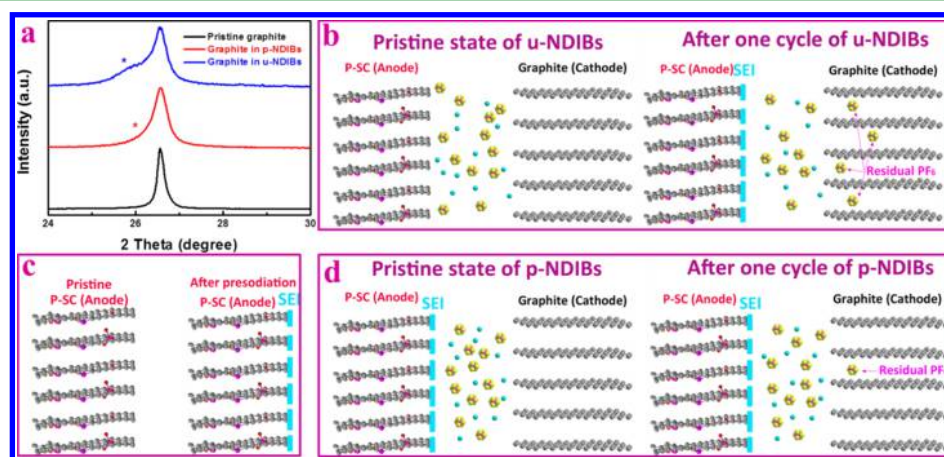


Figure 6. (a) XRD patterns of the graphite cathode at the state of pristine and after one cycle. (b) Proposed mechanism of the u-NDIBs after one cycle. (c) SEI formation during the presodiation process. (d) Proposed mechanism of the p-NDIBs after one cycle.

than that of u-NDIBs. In addition, when the current density is increased from 1000 to 3000 mA g⁻¹, the Coulombic efficiency is also improved to 95–99.99%. Again, when the current density returned back to 500 mA g⁻¹, a relative high Coulombic efficiency of 95% still could be obtained. The corresponding charge/discharge profiles of the p-NDIBs at various current densities are shown in Figure S13b. It should be noted that the superior electrochemical properties of p-NDIBs are comparable to the previous work (Table S2). Besides, the cycle performance of the NDIBs with the SC anode before and after anode presodiation was also performed. As shown in Figure S14, the NDIB after presodiation exhibits more stable cycle performance than that without presodiation, which also further demonstrated the favorable influence of the anode presodiation process on the cycle stability of NDIBs.

To investigate the mechanism of the significant improvement in electrochemical performance for NDIBs after presodiation, SEM and XPS measurements of the P-SC electrode of NDIBs and SIBs after the initial cycle were conducted (Figure 5). The SEM images of the P-SC electrode (Figure 5a–c) after the initial cycle revealed the formation of the SEI. In addition, the XPS measurements (Figure 5d,e) were conducted to confirm the SEI on the surface of the P-SC electrode. The distinct peaks of F 1s and Na 1s were observed for the both P-SC electrodes in the full survey XPS curves, and the atomic ratio of the F/Na is 20.87%:23.03% and 21.81%:21.31% for the P-SC electrode after presodiation and after the initial cycle of NDIBs, respectively. Moreover, the high-resolution F 1s XPS of the P-SC reflected that the F element for P-SC was from NaF although there was little PF₆⁻ in the P-SC electrode of NDIBs

after the initial cycles. In other words, the formation of NaF during the SEI formation consumed the Na⁺ in the electrolyte, which might break the balance of the Na⁺ and PF₆⁻ in the electrolyte.

In addition, the XRD measurements for graphite cathode were conducted after one cycle for the u-NDIBs and p-NDIBs (Figure 6a) to investigate the influence of the initial sodium loss which was offset by anode presodiation. It was obvious that the graphite was almost fully recovered for the p-NDIBs, while there was still a humpy peak around 26° for the u-NDIBs. The XRD humpy peak around 26° for the u-NDIBs was probably due to the PF₆⁻ residues in the graphite cathode. This was attributed to the SEI formation during the initial charge process of the u-NDIBs, resulting in large amount of sodium loss and thus the PF₆⁻ residues left in the graphite (Figure 6b). On the other hand, for the p-NDIBs, the SEI had formed during the presodiation process (Figure 6c), which could avoid the large amount sodium loss during cycling. Consequently, most of the PF₆⁻ in p-NDIBs could be deserted from the graphite cathode during discharge process, and the graphite would recover more readily (Figure 6d).

4. CONCLUSION

In summary, we have synthesized a high capacity P-SC anode and demonstrated a valid approach to offset the initial sodium loss via anode presodiation for high performance sodium-based DIBs. The NDIBs with the pre-sodiation process deliver high discharge capacity, excellent rate performance, superior Coulombic efficiency (p-NDIBs vs u-NDIBs: 95 vs 75% after a few cycles at 500 mA h g⁻¹), and long-term cycling stability (p-NDIBs vs u-NDIBs: 81 mA h g⁻¹ at 1000 mA g⁻¹ after 900 cycles with capacity retention of 81.8% vs 44 mA h g⁻¹ after 400 cycles at 1000 mA g⁻¹ with a capacity retention of 47.8%). This work provided a facile method to improve the anode capacity by phosphorus doping and also demonstrated an efficient way to offset the initial sodium loss.

■ ASSOCIATED CONTENT

Supporting Information

The Supporting Information is available free of charge on the ACS Publications website at DOI: 10.1021/acsami.8b03648.

SEM and TEM morphology, HRTEM morphology, XRD pattern, Raman and XPS analyses, nitrogen sorption and pore diameter analysis, DOS results, CV curves, discharge/charge profiles, Nyquist plots, cycle performance, summary of some reported carbonaceous anode materials for SIBs, and summary of the dual carbonaceous electrode for NDIBs (PDF)

■ AUTHOR INFORMATION

Corresponding Authors

*E-mail: fanling@hnu.edu.cn (L.F.).

*E-mail: qinyong@sxicc.ac.cn (Y.Q.).

*E-mail: luba2012@hnu.edu.cn (B.L.).

ORCID

Ling Fan: 0000-0002-4813-3895

Yong Qin: 0000-0002-5567-1464

Bingan Lu: 0000-0002-0075-5898

Author Contributions

^{||}R.M. and L.F. contributed equally to this work.

Notes

The authors declare no competing financial interest.

■ ACKNOWLEDGMENTS

This work was financially supported by National Natural Science Foundation of China (nos. 51672078 and 21473052) and Hunan University State Key Laboratory of Advanced Design and Manufacturing for Vehicle Body Independent Research Project (no. 71675004), Hunan Youth Talents (2016RS3025), and Foundation of State Key Laboratory of Coal Conversion (grant no. J17-18-903).

■ REFERENCES

- (1) Grey, C. P.; Tarascon, J. M. Sustainability and in situ monitoring in battery development. *Nat. Mater.* **2016**, *16*, 45–56.
- (2) Luo, W.; Shen, F.; Bommier, C.; Zhu, H.; Ji, X.; Hu, L. Na-Ion Battery Anodes: Materials and Electrochemistry. *Acc. Chem. Res.* **2016**, *49*, 231–240.
- (3) Wang, X.; Fan, L.; Gong, D.; Zhu, J.; Zhang, Q.; Lu, B. Core-Shell Ge@Graphene@TiO₂ Nanofibers as a High-Capacity and Cycle-Stable Anode for Lithium and Sodium Ion Battery. *Adv. Funct. Mater.* **2016**, *26*, 1104–1111.
- (4) Liu, Y.; Zhang, N.; Jiao, L.; Tao, Z.; Chen, J. Ultrasmall Sn Nanoparticles Embedded in Carbon as High-Performance Anode for Sodium-Ion Batteries. *Adv. Funct. Mater.* **2015**, *25*, 214–220.
- (5) Sharma, N.; Gonzalo, E.; Pramudita, J. C.; Han, M. H.; Brand, H. E. A.; Hart, J. N.; Pang, W. K.; Guo, Z.; Rojo, T. The Unique Structural Evolution of the O₃-Phase Na_{2/3}Fe_{2/3}Mn_{1/3}O₂ during High Rate Charge/Discharge: A Sodium-Centred Perspective. *Adv. Funct. Mater.* **2015**, *25*, 4994–5005.
- (6) Clément, R. J.; Billaud, J.; Armstrong, A. R.; Singh, G.; Rojo, T.; Bruce, P. G.; Grey, C. P. Structurally stable Mg-doped P₂-Na_{2/3}Mn_{1-y}Mg_yO₂ sodium-ion battery cathodes with high rate performance: insights from electrochemical, NMR and diffraction studies. *Energy Environ. Sci.* **2016**, *9*, 3240–3251.
- (7) Licht, S.; Douglas, A.; Ren, J.; Carter, R.; Lefler, M.; Pint, C. L. Carbon Nanotubes Produced from Ambient Carbon Dioxide for Environmentally Sustainable Lithium-Ion and Sodium-Ion Battery Anodes. *ACS Cent. Sci.* **2016**, *2*, 162–168.
- (8) Liu, Z.; Yu, X.-Y.; Lou, X. W.; Paik, U. Sb@C coaxial nanotubes as a superior long-life and high-rate anode for sodium ion batteries. *Energy Environ. Sci.* **2016**, *9*, 2314–2318.
- (9) Shiva, K.; Singh, P.; Zhou, W.; Goodenough, J. B. NaFe₂PO₄(SO₄)₂: a potential cathode for a Na-ion battery. *Energy Environ. Sci.* **2016**, *9*, 3103–3106.
- (10) Zhang, Z.; Zhang, Q.; Shi, J.; Chu, Y. S.; Yu, X.; Xu, K.; Ge, M.; Yan, H.; Li, W.; Gu, L.; Hu, Y.-S.; Li, H.; Yang, X.-Q.; Chen, L.; Huang, X. A Self-Forming Composite Electrolyte for Solid-State Sodium Battery with Ultralong Cycle Life. *Adv. Energy Mater.* **2017**, *7*, 1601196.
- (11) Gong, D.; Wang, B.; Zhu, J.; Podila, R.; Rao, A. M.; Yu, X.; Xu, Z.; Lu, B. An Iodine Quantum Dots Based Rechargeable Sodium-Iodine Battery. *Adv. Energy Mater.* **2017**, *7*, 1601885.
- (12) Fan, L.; Liu, Q.; Chen, S.; Lin, K.; Xu, Z.; Lu, B. Potassium-Based Dual Ion Battery with Dual-Graphite Electrode. *Small* **2017**, *13*, 1701011.
- (13) Fan, L.; Liu, Q.; Xu, Z.; Lu, B. An Organic Cathode for Potassium Dual-Ion Full Battery. *ACS Energy Lett.* **2017**, *2*, 1614–1620.
- (14) Fan, L.; Lin, K.; Wang, J.; Ma, R.; Lu, B. A Nonaqueous Potassium-Based Battery-Supercapacitor Hybrid Device. *Adv. Mater.* **2018**, *30*, 1800804.
- (15) Fan, L.; Ma, R.; Yang, Y.; Chen, S.; Lu, B. Covalent sulfur for advanced room temperature sodium-sulfur batteries. *Nano Energy* **2016**, *28*, 304–310.
- (16) Manthiram, A.; Yu, X. Ambient temperature sodium-sulfur batteries. *Small* **2015**, *11*, 2108–2114.

- (17) Kohl, M.; Borrmann, F.; Althues, H.; Kaskel, S. Hard Carbon Anodes and Novel Electrolytes for Long-Cycle-Life Room Temperature Sodium-Sulfur Full Cell Batteries. *Adv. Energy Mater.* **2016**, *6*, 1502185.
- (18) Wei, S.; Xu, S.; Agrawal, A.; Choudhury, S.; Lu, Y.; Tu, Z.; Ma, L.; Archer, L. A. A stable room-temperature sodium-sulfur battery. *Nat. Commun.* **2016**, *7*, 11722.
- (19) Seel, J. A.; Dahn, J. R. Electrochemical intercalation of PF₆ into graphite. *J. Electrochem. Soc.* **2000**, *147*, 892–898.
- (20) Read, J. A.; Cresce, A. V.; Ervin, M. H.; Xu, K. Dual-graphite chemistry enabled by a high voltage electrolyte. *Energy Environ. Sci.* **2014**, *7*, 617–620.
- (21) Rothermel, S.; Meister, P.; Schmuelling, G.; Fromm, O.; Meyer, H.-W.; Nowak, S.; Winter, M.; Placke, T. Dual-graphite cells based on the reversible intercalation of bis(trifluoromethanesulfonyl)imide anions from an ionic liquid electrolyte. *Energy Environ. Sci.* **2014**, *7*, 3412–3423.
- (22) Aubrey, M. L.; Long, J. R. A Dual-Ion Battery Cathode via Oxidative Insertion of Anions in a Metal-Organic Framework. *J. Am. Chem. Soc.* **2015**, *137*, 13594–13602.
- (23) Bordet, F.; Ahlbrecht, K.; Tübke, J.; Ufheil, J.; Hoes, T.; Oetken, M.; Holzapfel, M. Anion intercalation into graphite from a sodium-containing electrolyte. *Electrochim. Acta* **2015**, *174*, 1317–1323.
- (24) Sheng, M.; Zhang, F.; Ji, B.; Tong, X.; Tang, Y. A Novel Tin-Graphite Dual-Ion Battery Based on Sodium-Ion Electrolyte with High Energy Density. *Adv. Energy Mater.* **2017**, *7*, 1601963.
- (25) Zhang, F.; Ji, B.; Tong, X.; Sheng, M.; Zhang, X.; Lee, C.-S.; Tang, Y. A Dual-Ion Battery Constructed with Aluminum Foil Anode and Mesocarbon Microbead Cathode via an Alloying/Intercalation Process in an Ionic Liquid Electrolyte. *Adv. Mater. Interfaces* **2016**, *3*, 1600605.
- (26) Zhang, X.; Tang, Y.; Zhang, F.; Lee, C.-S. A Novel Aluminum-Graphite Dual-Ion Battery. *Adv. Energy Mater.* **2016**, *6*, 1502588.
- (27) Ji, B.; Zhang, F.; Song, X.; Tang, Y. A Novel Potassium-Ion-Based Dual-Ion Battery. *Adv. Mater.* **2017**, *29*, 1700519.
- (28) Ji, B.; Zhang, F.; Wu, N.; Tang, Y. A Dual-Carbon Battery Based on Potassium-Ion Electrolyte. *Adv. Energy Mater.* **2017**, *7*, 1700920.
- (29) Jiang, C.; Fang, Y.; Lang, J.; Tang, Y. Integrated Configuration Design for Ultrafast Rechargeable Dual-Ion Battery. *Adv. Energy Mater.* **2017**, *7*, 1700913.
- (30) Qin, P.; Wang, M.; Li, N.; Zhu, H.; Ding, X.; Tang, Y. Bubble-Sheet-Like Interface Design with an Ultrastable Solid Electrolyte Layer for High-Performance Dual-Ion Batteries. *Adv. Mater.* **2017**, *29*, 1606805.
- (31) Rodríguez-Pérez, I. A.; Ji, X. Anion Hosting Cathodes in Dual-Ion Batteries. *ACS Energy Lett.* **2017**, *2*, 1762–1770.
- (32) Zhu, H.; Zhang, F.; Li, J.; Tang, Y. Penne-Like MoS₂/Carbon Nanocomposite as Anode for Sodium-Ion-Based Dual-Ion Battery. *Small* **2018**, *14*, 1703951.
- (33) Wang, P.-F.; You, Y.; Yin, Y.-X.; Wang, Y.-S.; Wan, L.-J.; Gu, L.; Guo, Y.-G. Suppressing the P2-O2 Phase Transition of Na_{0.67}Mn_{0.67}Ni_{0.33}O₂ by Magnesium Substitution for Improved Sodium-Ion Batteries. *Angew. Chem., Int. Ed.* **2016**, *55*, 7445–7449.
- (34) You, Y.; Wu, X.-L.; Yin, Y.-X.; Guo, Y.-G. High-quality Prussian blue crystals as superior cathode materials for room-temperature sodium-ion batteries. *Energy Environ. Sci.* **2014**, *7*, 1643–1647.
- (35) You, Y.; Kim, S. O.; Manthiram, A. A Honeycomb-Layered Oxide Cathode for Sodium-Ion Batteries with Suppressed P₃-O₁ Phase Transition. *Adv. Energy Mater.* **2017**, *7*, 1601698.
- (36) You, Y.; Manthiram, A. Progress in High-Voltage Cathode Materials for Rechargeable Sodium-Ion Batteries. *Adv. Energy Mater.* **2018**, *8*, 1701785.
- (37) Shi, X.; Zhang, W.; Wang, J.; Zheng, W.; Huang, K.; Zhang, H.; Feng, S.; Chen, H. (EMIm)⁺(PF₆)⁻ Ionic Liquid Unlocks Optimum Energy/Power Density for Architecture of Nanocarbon-Based Dual-Ion Battery. *Adv. Energy Mater.* **2016**, *6*, 1601378.
- (38) Ishihara, T.; Koga, M.; Matsumoto, H.; Yoshio, M. Electrochemical intercalation of hexafluorophosphate anion into various carbons for cathode of dual-carbon rechargeable battery. *Electrochem. Solid-State Lett.* **2007**, *10*, A74–A76.
- (39) Rodríguez-Pérez, I. A.; Jian, Z.; Waldenmaier, P. K.; Palmisano, J. W.; Chandrasekhar, R. S.; Wang, X.; Lerner, M. M.; Carter, R. G.; Ji, X. A Hydrocarbon Cathode for Dual-Ion Batteries. *ACS Energy Lett.* **2016**, *1*, 719–723.
- (40) Tong, X.; Zhang, F.; Ji, B.; Sheng, M.; Tang, Y. Carbon-Coated Porous Aluminum Foil Anode for High-Rate, Long-Term Cycling Stability, and High Energy Density Dual-Ion Batteries. *Adv. Mater.* **2016**, *28*, 9979–9985.
- (41) Zhang, X.; Tang, Y.; Zhang, F.; Lee, C.-S. A Novel Aluminum-Graphite Dual-Ion Battery. *Adv. Energy Mater.* **2016**, *6*, 1502588.
- (42) Fan, L.; Liu, Q.; Chen, S.; Xu, Z.; Lu, B. Soft Carbon as Anode for High-Performance Sodium-Based Dual Ion Full Battery. *Adv. Energy Mater.* **2017**, *7*, 1602778.
- (43) Zhang, J.; Yin, Y.-X.; Guo, Y.-G. High-Capacity Te Anode Confined in Microporous Carbon for Long-Life Na-Ion Batteries. *ACS Appl. Mater. Interfaces* **2015**, *7*, 27838–27844.
- (44) Wang, P.-F.; You, Y.; Yin, Y.-X.; Guo, Y.-G. An O₃-type NaNi_{0.5}Mn_{0.5}O₂ cathode for sodium-ion batteries with improved rate performance and cycling stability. *J. Mater. Chem. A* **2016**, *4*, 17660–17664.
- (45) Yan, Y.; Yin, Y.-X.; Guo, Y.-G.; Wan, L.-J. A Sandwich-Like Hierarchically Porous Carbon/Graphene Composite as a High-Performance Anode Material for Sodium-Ion Batteries. *Adv. Energy Mater.* **2014**, *4*, 1301584.
- (46) You, Y.; Yao, H.-R.; Xin, S.; Yin, Y.-X.; Zuo, T.-T.; Yang, C.-P.; Guo, Y.-G.; Cui, Y.; Wan, L.-J.; Goodenough, J. B. Subzero-Temperature Cathode for a Sodium-Ion Battery. *Adv. Mater.* **2016**, *28*, 7243–7248.
- (47) de la Llave, E.; Borgel, V.; Park, K.-J.; Hwang, J.-Y.; Sun, Y.-K.; Hartmann, P.; Chesneau, F.-F.; Aurbach, D. Comparison between Na-Ion and Li-Ion Cells: Understanding the Critical Role of the Cathodes Stability and the Anodes Pretreatment on the Cells Behavior. *ACS Appl. Mater. Interfaces* **2016**, *8*, 1867–1875.
- (48) Oh, S.-M.; Myung, S.-T.; Hwang, J.-Y.; Scrosati, B.; Amine, K.; Sun, Y.-K. High Capacity O₃-Type Na[Li_{0.05}(Ni_{0.25}Fe_{0.25}Mn_{0.5})_{0.95}]O₂ Cathode for Sodium Ion Batteries. *Chem. Mater.* **2014**, *26*, 6165–6171.
- (49) Jian, Z.; Hwang, S.; Li, Z.; Hernandez, A. S.; Wang, X.; Xing, Z.; Su, D.; Ji, X. Hard-Soft Composite Carbon as a Long-Cycling and High-Rate Anode for Potassium-Ion Batteries. *Adv. Funct. Mater.* **2017**, *27*, 1700324.
- (50) Luo, W.; Jian, Z.; Xing, Z.; Wang, W.; Bommier, C.; Lerner, M. M.; Ji, X. Electrochemically Expandable Soft Carbon as Anodes for Na-Ion Batteries. *ACS Cent. Sci.* **2015**, *1*, 516–522.
- (51) Möbus, M.; Karl, N.; Kobayashi, T. Structure of perylene-tetracarboxylic-dianhydride thin films on alkali halide crystal substrates. *J. Cryst. Growth* **1992**, *116*, 495–504.
- (52) Yin, L.; Wang, Y.; Han, C.; Kang, Y.-M.; Ma, X.; Xie, H.; Wu, M. Self-assembly of disordered hard carbon/graphene hybrid for sodium-ion batteries. *J. Power Sources* **2016**, *305*, 156–160.
- (53) Ma, X.; Ning, G.; Qi, C.; Xu, C.; Gao, J. Phosphorus and nitrogen dual-doped few-layered porous graphene: a high-performance anode material for lithium-ion batteries. *ACS Appl. Mater. Interfaces* **2014**, *6*, 14415–14422.
- (54) Zhang, C.; Mahmood, N.; Yin, H.; Liu, F.; Hou, Y. Synthesis of phosphorus-doped graphene and its multifunctional applications for oxygen reduction reaction and lithium ion batteries. *Adv. Mater.* **2013**, *25*, 4932–4937.
- (55) Li, Y.; Yuan, Y.; Bai, Y.; Liu, Y.; Wang, Z.; Li, L.; Wu, F.; Amine, K.; Wu, C.; Lu, J. Insights into the Na⁺ Storage Mechanism of Phosphorus-Functionalized Hard Carbon as Ultrahigh Capacity Anodes. *Adv. Energy Mater.* **2018**, *8*, 1702781.
- (56) Fan, L.; Lu, B. Reactive Oxygen-Doped 3D Interdigitated Carbonaceous Materials for Li and Na Ion Batteries. *Small* **2016**, *12*, 2783–2791.



Confined and covalent sulfur for stable room temperature potassium-sulfur battery

Ruifang Ma^{a,1}, Ling Fan^{a,1}, Jue Wang^a, Bingan Lu^{a,b,c,d,*}

^a School of Physics and Electronics, Hunan University, Changsha, 410082, China

^b State Key Laboratory of Coal Conversion, Institute of Coal Chemistry, Chinese Academy of Sciences, Shanxi, 030001, China

^c Material Technology Company Limited, Wing Lok Street, Sheung Wan, 999077 Hong Kong, China

^d Fujian Strait Research Institute of Industrial Graphene Technologies, Jinjiang, 362200, China

ARTICLE INFO

Article history:

Received 6 September 2018

Received in revised form

30 September 2018

Accepted 7 October 2018

Available online 8 October 2018

Keywords:

Confined and covalent sulfur

Potassium sulfur battery

Room temperature

High energy

Electrochemistry

ABSTRACT

Potassium-sulfur (K-S) battery represents one of the most promising electrochemical energy storage devices because of the low cost and abundance of potassium and sulfur resources, but the inferior cycle stability and high operating temperature seriously impede its applications. Herein, a high energy and stable room temperature K-S battery was developed with a confined ad covalent sulfur cathode, which could deliver an energy density as high as $\sim 445 \text{ Wh Kg}^{-1}$, a Coulombic efficiency close to 100%, and a superior cycle stability with a capacity retention of 86.3% over 300 cycles at a voltage cut-off of 0.8–3.0 V. This work displayed a basic study on the rechargeable potassium-sulfur batteries and may pave the way for designing sulfur based electrode materials for potassium based ion batteries.

© 2018 Elsevier Ltd. All rights reserved.

1. Introduction

Lithium ion batteries have been commercialized for decades since their first launch by Sony in the early 1990s and are becoming more and more popular in our daily life. However, the limited lithium resources and high cost of lithium ion batteries have aroused severe concerns over their long-term development [1]. Therefore, tremendous efforts have been dedicated to exploring alternative rechargeable metal ion batteries, including potassium ion batteries (PIBs) [2–27], sodium ion batteries (SIBs) [28–33], magnesium ion batteries (MIBs) [34], and aluminum ion batteries (AIBs) [35]. Among them, PIBs are considered one of the most promising rechargeable batteries, not only due to the plenty and low cost of potassium resources, but also the benefits coming from the lower standard electrode potential of K ($-2.93 \text{ V vs. } E^0$) compared with Na ($-2.71 \text{ V vs. } E^0$), Mg ($-2.37 \text{ V vs. } E^0$), and Al ($-1.66 \text{ V vs. } E^0$), implying that the PIBs may possess a higher energy density and a higher discharge voltage in comparison to SIBs, MIBs

and AIBs. In addition, sulfur, one of the most efficient cathode materials due to its high capacity and inexpensiveness, has been vigorously investigated in lithium-sulfur (Li-S) batteries and sodium-sulfur (Na-S) batteries [36–49]. Despite of that, the study on potassium-sulfur (K-S) batteries is still in the infancy stage. Therefore, investigation and development of potassium-sulfur (K-S) batteries through incorporating the sulfur electrode into potassium batteries are highly demanded.

K-S batteries are facing the same problem as Li-S and Na-S batteries, the infamous shuttle effect (the transport of soluble polysulfides between cathode and anode), which leads to an inferior Coulombic efficiency and a rapid capacity decay. Besides, the radius of potassium ion (133 pm) is much larger than that of lithium ion (76 pm) and sodium ion (102 pm), causing a huge volume expansion during potassiation/depotassiation processes and possibly destroying the electrode materials, which further deteriorates the electrochemical performance. Even though K-S batteries have been reported by Chen group and Lu group, their poor cycle stability and high operating temperature remain the big challenges [50,51]. Therefore, it is urgent to develop K-S batteries which have a better cycle stability and are able to work at room temperature. Besides, the sulfur in the previously K-S batteries are main S_8 or K_2S_n , which will result in serious shuttle effect just like

* Corresponding author. School of Physics and Electronics, Hunan University, Changsha, 410082, China.

E-mail address: luba2012@hnu.edu.cn (B. Lu).

¹ These authors contributed equally to this work.

Li-S and Na-S batteries, and the performance will be restricted [50,52]. Drawing on the experience of Li-S and Na-S batteries, the performance of metal-sulfur batteries could be significantly enhanced by confining sulfur in carbon materials or choosing covalent sulfur as the sulfur host materials [40,53–55]. Therefore, covalent sulfur confined in the host was employed to improve the electrochemical performance of K-S batteries.

Herein, we reported a stable room temperature K-S battery, which was assembled using 1M potassium trifluoromethanesulfonate (KSO_3CF_3) in ethylene carbonate: diethyl carbonate (EC:DEC, 1:1 v/v) as the electrolyte, confined and covalent sulfur cathode (CCS, 39.25% sulfur content) as the sulfur host material, and potassium foil as the anode. Most excitingly, no shuttle effect was observed in the K-S batteries, benefiting from the covalent and confined sulfur in the CCS as well as the carbonate electrolyte. Besides, with a cut-off voltage range from 3.0 V to 0.8 V, the morphology of CCS was well maintained. Hence, the K-S batteries, as expected, delivered a high reversible capacity of 343 mA h g^{-1} (calculated based on the total weight of CCS cathode), a high energy density of $\sim 455 \text{ Wh Kg}^{-1}$, a stable cyclability over 300 cycles, a superior capacity retention of 86.3%, and a high Coulombic efficiency around 100%.

2. Experimental section

2.1. Material synthesis

2.1.1. Synthesis of confined and covalent sulfur (CCS)

All chemicals were used as received without further purification. Polyacrylonitrile (M_w :150000) was purchased from Sigma-Aldrich. KSO_3CF_3 , ethyl carbonate, and diethyl carbonate were purchased from BASF. The CCS materials was synthesized according to a previously described method [48]. Typically, annealing the polyacrylonitrile and sulfur (weight ratio of 1:3) at 350°C , 450°C and 550°C for 10 h with a heating rate of 5°C min^{-1} under Ar. For comparison purposes, CCS based carbonaceous materials were prepared by annealing the polyacrylonitrile at 350°C , 450°C or 550°C for 10 h with a heating rate of 5°C min^{-1} under Ar.

2.1.2. Preparation of electrolyte

The electrolyte was prepared by dissolving KSO_3CF_3 (0.75 g) in the solvents of 2 ml ethyl carbonate (EC) and 2 ml diethyl carbonate (DEC) (1:1, v/v), and then stirred for over 6 h before usage. The ether based electrolyte was prepared by dissolving 0.75 g KSO_3CF_3 in 4 ml DME.

2.2. Material characterizations

The morphology of the CCS was characterized by Titan G2 60-300 TEM and Hitachi S-4800 SEM. XRD patterns were recorded by Philips, X'pert pro with a $\text{Cu K}\alpha = 0.154056 \text{ nm}$. Raman spectra were measured with Renishaw 2000. XPS measurements were investigated by ESCALAB 250Xi. BET surface area measurements were performed with a Micromeritics ASAP 2020 surface area and porosity analyzer.

2.3. Electrochemical measurements

The CCS electrode was fabricated as follows: CCS based carbonaceous materials, carbon black, and carboxyl methyl cellulose with a weight ratio of 8:1:1 were dissolved into the solution of $\text{C}_2\text{H}_5\text{OH}$ and deionized water (1:3, w/w), and stirred for over 8 h before spreading them onto an aluminum foil. Then let it dry at 80°C in oven for over 24 h (as the sulfur is covalent and confined, the 80°C drying process will not lead to obvious sulfur loss). The

average areal weight loading of the CCS materials was about $1.0\text{--}1.5 \text{ mg cm}^{-2}$. All the potassium-sulfur 2032 type coin cells were assembled in glovebox under Ar with CCS as the cathode, potassium foil as the anode, 1M KSO_3CF_3 in EC:DEC (1:1, v/v) or 1 M KSO_3CF_3 in DME as the electrolyte, and Whatman glass fiber as the separator. The dosage of electrolyte for each coin cell is around $120 \mu\text{l}$. The galvanostatic charge/discharge and rate performance of the K-S batteries were performed by Arbin Instrument BT 2000 model. Electrochemical workstation was used to investigate the cyclic voltammograms (CV) of the K-S batteries with a scan rate of 0.2 mV s^{-1} and a voltage range of 3.0–0.1 V.

To test the cycled electrodes, the K-S batteries were disassembled followed by washing the electrodes with DEC for twice to remove the potassium salt. All the operations were conducted in the glove box.

Calculation of the theoretical capacity of the K-S batteries with CCS annealed at 450°C as cathodes with 0.8–3.0 V: it could be found that the capacity of the carbon derived from pure polyacrylonitrile is negligible when the discharge cut-off is over 0.5 V (Fig. S6). Therefore, we calculated the theoretical capacity of CCS annealed at 450°C based on the sulfur content (39.25%). Assumption that the S could be fully reduced to S^{2-} and formation of K_2S , the theoretical capacity is $C_{\text{the}} = 1675 \text{ mA h g}^{-1} \times 39.25\% = 657 \text{ mA h g}^{-1}$. Assumption that the S could be reduced to S_2^{2-} and formation of K_2S_2 , the theoretical capacity is $C_{\text{the}} = 1675 \text{ mA h g}^{-1} \times 0.5 \times 39.25\% = 328.5 \text{ mA h g}^{-1}$. Assumption that the S could be reduced to S_3^{2-} and formation of K_2S_3 , the theoretical capacity is $C_{\text{the}} = 1675 \text{ mA h g}^{-1} \times 0.3333 \times 39.25\% = 219.1 \text{ mA h g}^{-1}$. Nonetheless, the theoretical capacity is $219.1 \text{ mA h g}^{-1} \leq C_{\text{the}} \leq 657 \text{ mA h g}^{-1}$ when the final production is the mixture of K_2S , K_2S_2 , and K_2S_3 . The energy density values E (Wh kg^{-1}) were calculated as: $E = C_d \cdot V_d$, where C_d represents for the discharge capacity, V_d represents for the medium discharge voltage.

3. Results and discussion

The confined and covalent sulfur (CCS) was prepared by thermally annealing the polyacrylonitrile and sulfur at 350°C , 450°C and 550°C for 10 h. Fig. 1 exhibits the characteristics of the CCS. It can be seen that CCS@ 450°C (Fig. 1a and b) is mainly comprised of spherical nanoparticles. There is no apparent lattice fringe in the high-resolution transmission electron microscope (HRTEM) image (Fig. 1c), indicating that the CCS@ 450°C is polycrystalline, which is further confirmed by the rings observed in the SAED pattern (Fig. 1c inset). Besides, the elemental mappings (Fig. 1d) exhibit a homogenous distribution of sulfur, carbon, and nitrogen in the nanoparticles. Moreover, the sulfur content calculated from the elemental mapping is 38.6%, consistent with the element analysis (39.25%), suggesting a homogenous distribution of sulfur in the CCS.

To evaluate the total specific surface area (SSA) of CCS at different temperature, nitrogen adsorption/desorption isotherms measurements were conducted. The specific surface area of CCS@ 450°C was $14.2744 \text{ m}^2 \text{ g}^{-1}$, with the pore diameters (Supplementary Fig. S1d) of 2–7 nm. As comparison, the specific surface area of CCS@ 350°C and CCS@ 550°C was $13.8796 \text{ m}^2 \text{ g}^{-1}$ and $5.6779 \text{ m}^2 \text{ g}^{-1}$, with the pore diameters around 2–5 nm and 10–50 nm (Supplementary Fig. S1b and S1f). The low surface area of CCSs indicated the close packing of CCS, which was beneficial for obtaining high volumetric energy density.

The Fourier transform infrared spectroscopy (FTIR) spectra (Fig. 1e) of the three composites display similar characteristic peaks, except for the gradually weakened peaks of S-S bond (933 cm^{-1} and 510 cm^{-1}) with the rising of annealing temperature [55]. In addition, the existence of C-S bond (661 cm^{-1}) along with S-

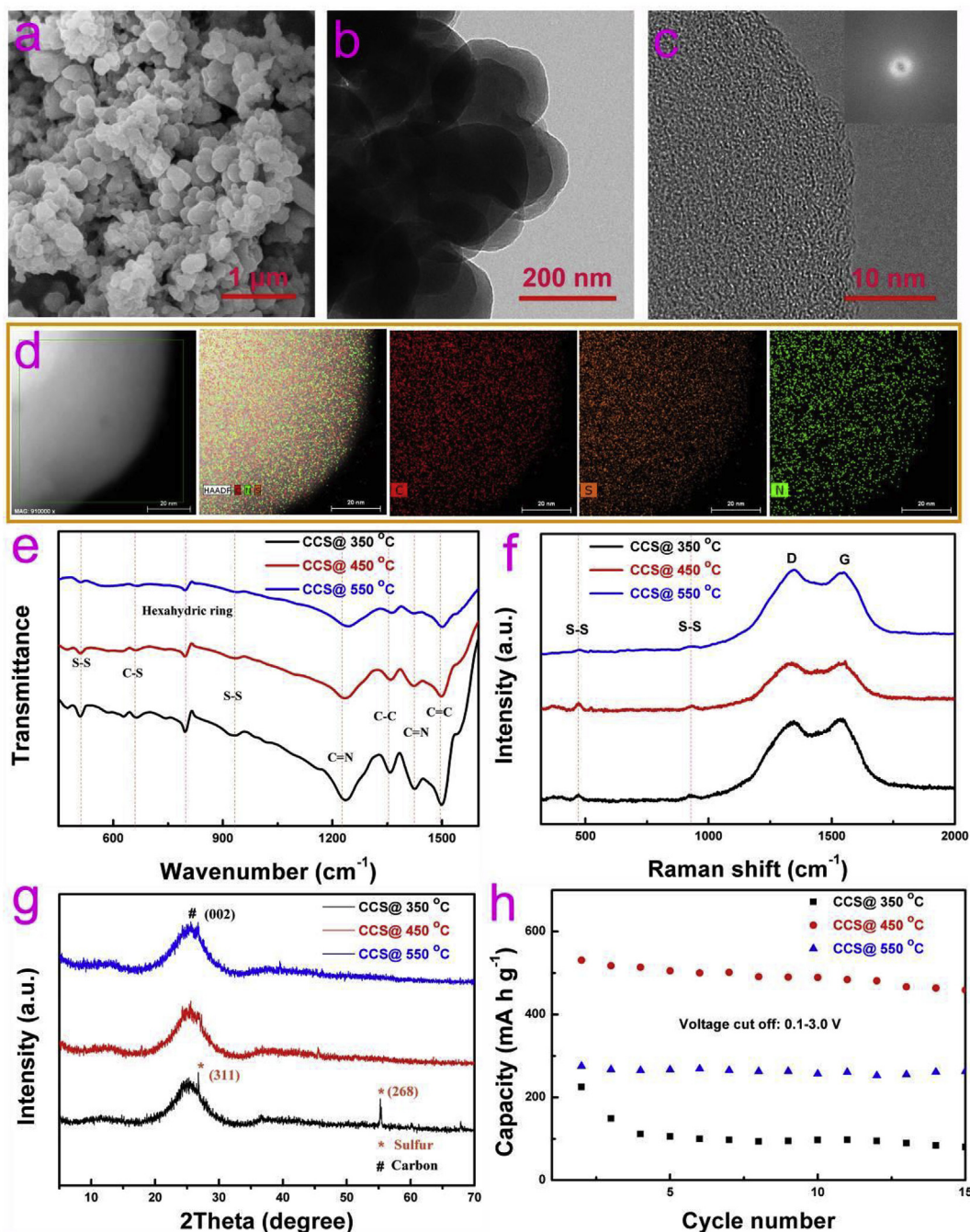


Fig. 1. Morphology and structure characterization of the sulfur cathode. a) SEM image. b) TEM image. c) HRTEM image, inset: SAED pattern. d) Elemental mapping. e) FTIR spectra. f) Raman spectra. g) XRD patterns. h) Cycle performance of CCS annealed at different temperature.

S bond offers a strong evidence to prove that the sulfur element forms covalent bonds in the CCS. Furthermore, the Raman spectra (Fig. 1f) also demonstrate the existence of S-S bonds (470 cm^{-1} and 926 cm^{-1}) in the CCS materials. The XRD patterns in Fig. 1g display one peak at around 25.5° , which could be assigned to the (0 0 2) plane of the disordered carbon. Meanwhile, two sharp peaks located at 26.7° and 55.2° are observed in CCS@ 350°C , corresponding to (3 1 1) and (2 6 8) facets of sulfur (S_8 ; PDF#74-1465). These results indicate that the sulfur in the CCS is confined and covalent, which is beneficial to the electrochemical performance.

Electrochemical performance of the three sulfur containing composites was evaluated. Fig. 1h presents the cycle performance

(starting from the second one) of the three composites at 150 mA g^{-1} with a voltage cut-off of 0.1–3.0 V using 1M KSO_3CF_3 in EC: DEC (1:1 v/v) as electrolyte (the capacity is calculated based on the total weight of active materials). It is clear that the capacity of the CCS annealed at 350°C is relatively low and its cycle stability is inferior because of the high sulfur content and low conductivity; while for the CCS treated at 550°C , the stability is impressive whereas the capacity is still relatively low, possibly due to the low sulfur content. Interestingly, the CCS annealed at 450°C delivers the highest capacity, possibly due to the suitable sulfur content and high conductivity (Supplementary Fig. S2). Besides, the batteries with 1M KSO_3CF_3 in DME electrolyte were also assembled as a

comparison (Supplementary Fig. S3), and the capacity is decreased rapidly compared with the carbonate electrolyte (Fig. 1h) due to the shuttle effect in the DME electrolyte. Therefore, the CCS@ 450 °C and the carbonate electrolyte was used in the following investigations.

Fig. 2a exhibits the charge-discharge profiles at 150 mA g⁻¹ with a voltage range of 0.1–3.0 V. It could deliver a discharge/charge capacity of 867/632 mA h g⁻¹, corresponding to an initial Coulombic efficiency of 72.9%. To investigate the products of the battery during discharge, ex-situ Raman, FTIR and XPS were performed. As illustrated in the ex-situ Raman spectra (Fig. 2b), the amount of S-S bond (470 cm⁻¹) varied during the discharge/charge process. Specially, the peak around 474 cm⁻¹ was broadened when the battery was discharged to 1.0 V, and two broad peaks around 364 cm⁻¹ and 565 cm⁻¹ appeared, which might be on account of the reduction of sulfur and formation of K₂S_n (2 < n < 8) [51,56].

When the battery was further discharged to 0.5 V, the peaks at 474 cm⁻¹, 364 cm⁻¹ and 565 cm⁻¹ disappeared and an obvious peak at around 449 cm⁻¹ emerged, which is probably from K₂S₂; moreover, a tiny peak located at 526 cm⁻¹ showed up, likely ascribed to the K₂S [51]. When the electrode was discharged to 0.1 V, there was no more change in the Raman spectra, indicating that the main sulfur reduction should be accomplished above 0.5 V and the reduction products of the electrode are mixtures of K₂S and K₂S₂. More importantly, the S-S bond recovered when the electrode was charged to 3.0 V, implying a superior reversibility of S-S bond. Thereafter, the ex-situ FTIR also confirmed the reversibility of S-S bond (Supplementary Fig. S4), which may yield an excellent electrochemical performance. And the high reversible S-S bonds is might be due to the sulfur in the CCS is covalent and confined [40]. In addition, according to the full survey XPS in Supplementary Fig. S5 and Fig. 2c, three distinct peaks at around ~165 eV, 293 eV,

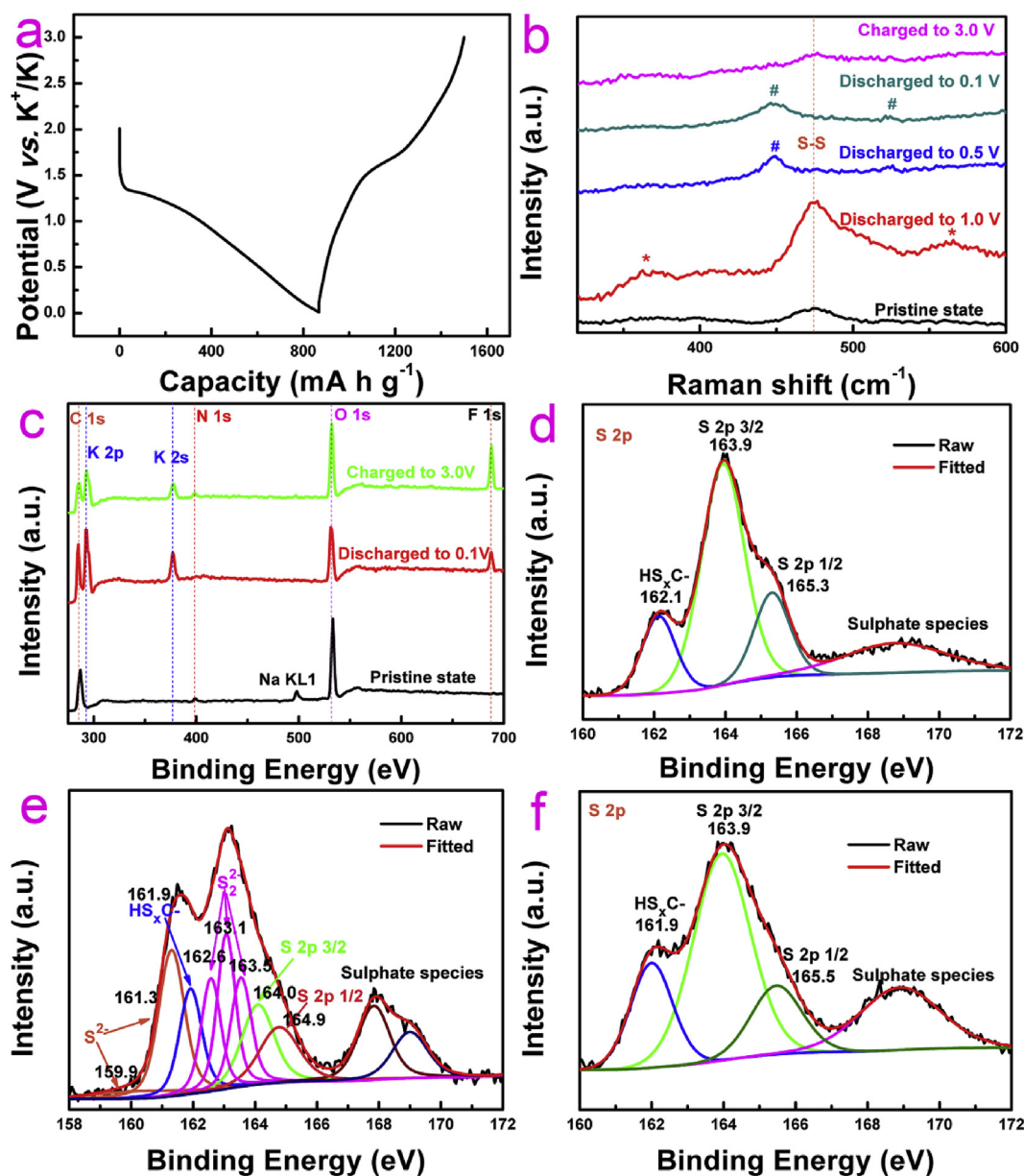


Fig. 2. a) The initial discharge-charge profile. b) The ex-situ Raman spectra of the electrode at different states during the initial cycle. (c-f) The XPS curves of the electrodes at different states during the initial cycle. c) Full survey XPS. d) Pristine state. e) Discharged to 0.1 V. f) Charged to 3.0 V.

377 eV and 688 eV were observed when the battery was discharged to 0.1 V, assigning of these peaks to S2p, K2p, K2s and F1s, respectively. Moreover, the intensity of K2p and K2s peaks decreased dramatically when the battery was charged to 3.0 V. For the purpose of understanding the reaction mechanism between S and K, the evolution of S chemical bond was analyzed. There are four peaks observed at 162.1 eV, 163.9 eV, 165.3 eV and 169 eV in the pristine state (Fig. 2d), corresponding to the bonds of HS_xC-, S 2p 3/2, S 2p 1/2, and sulphate species, respectively [55]. The S2p peak shifted to the lower energy when the battery was discharged to 0.1 V (Fig. 2e), standing for the reduction of S. Specially, the peaks at 159.9 eV and 161.3 eV represented for the S²⁻ derived from the K₂S product. In addition, three distinct peaks at around 162.6 eV, 163.1 eV and 163.5 eV are likely belonging to K₂S₂. The S2p shifted to the higher value with the battery being charged to 3.0 V (Fig. 2f), corresponding to the oxidation of sulfur species. The ex-situ S2p XPS spectra demonstrated the reversibility of sulfur species during potassiation/de-potassiation process, in agreement with the ex-situ Raman spectra.

Besides, transmission electron microscopy (TEM) elemental mapping and high resolution TEM (HRTEM) were conducted for a more intuitive understanding of the transformation of CCS during potassiation/de-potassiation process. Fig. 3a presents the pristine state of the CCS electrode. It is found that the distribution of C, S and N is uniform. But the content of K increased significantly when the electrode was discharged to 0.1 V (Fig. 3b). Considering the atomic ratio of S:K 1:1.43 at this stage, it tells that only a certain amount of S has been turned into K₂S, while the others exist in a higher oxidation state (K₂S₂). Additionally, the distribution of S and K elements in the electrode is almost identical, revealing that the capacity is primarily from the sulfur which reacts with K. As expected, the content of potassium was reduced considerably and the atomic ratio of S: K was enlarged to 1:0.22 when the battery was charged to 3.0 V (Fig. 3c), indicating the successful depotassiation during charge process. In a word, the ex-situ TEM elemental mappings have verified the reversibility of potassiation/de-potassiation process of the CCS cathode. The corresponding elemental compositions of the electrode calculated from TEM elemental mappings at different states during the initial cycle are shown in Supplementary Fig. S6. Moreover, HRTEM was used to probe the products of the CCS after the batteries were discharged to 0.1 V (Fig. 3d, e). Two types of highly ordered nanocrystalline with lattice distances of 0.300 nm and 0.368 nm were identified, indexed to the (-2 -2 2) and (2 0 0) planes of K₂S₂ (Fig. 3d). Besides, another nanocrystalline with a lattice spacing of 0.370 nm was also detected, corresponding to the (2 0 0) plane of K₂S (Fig. 3e). HRTEM has validated that the products of the battery discharged to 0.1 V are mixtures of K₂S and K₂S₂, consistent with the XPS measurements and TEM elemental mapping analysis.

Fig. 4a presents the cyclic voltammetry (CV) curves of the CCS electrode with a scan rate of 0.2 mV s⁻¹. A primary peak located at 0.81 V is observed during the initial discharge process, which could be assigned to the reaction between sulfur species and K⁺; besides, a small peak appears at 0.01 V, corresponding to the interaction between K⁺ and carbon. During the charge process, a prominent peak at 1.84 V and a small peak at 2.41 V could be noticed, which is related to the de-potassiation process and formation of sulfur species. Specially, the peak at 1.84 V could be ascribed to the formation of long-chain potassium polysulfides from short-chain potassium sulfides, and the peak at 2.41 V is assigned to the oxidation of potassium polysulfides into elemental sulfur. Besides, it can be perceived that the CV curve of the initial discharge process is very different from the subsequent cycles, which could be attributed the formation of solid electrolyte interphase (SEI) during the initial discharge process. During the subsequent cycles, there is a

downward sloping curve between 2.3 V and 1.2 V as well as a peak located at 0.83 V in the discharge process, which is attributed to the different reactions between sulfur and K⁺. The downward sloping curve between 2.3 V and 1.2 V is probably due to the transition from elemental sulfur to potassium polysulfides (K₂S_n, 2 < n < 6) and the peak located at 0.83 V is likely attributable to the formation of K₂S by further potassiation of the potassium polysulfide (K₂S_n, 2 ≤ n ≤ 3). Moreover, no obvious difference is found in the CV curves between the second and fifth cycles, displaying a superior reversibility during charge/discharge process.

The cycle performance of the CCS was investigated at a current density of 150 mA g⁻¹ with various discharge cut-off voltages. As shown in Fig. 4b,c, the battery could deliver a reversible capacity of 574 mA h g⁻¹ when the cut-off voltage was 0.1 V; but it only delivered a reversible capacity of 117 mA h g⁻¹ after 200 cycles, equivalent to a capacity retention of 20.4% and 0.398% decay per cycle. The severe capacity decay of the CCS might be caused by the large volume expansion during the potassiation process, resulting in the structure destruction and pulverization and then leading to inferior cycle stability. Since the volume expansion is in proportion to the degree of potassiation of the CCS electrode, we assume that this issue can be addressed through modulating the potassiation level of the CCS electrode, which could be straightforwardly achieved by controlling the discharge cut-off voltage. Therefore, a higher discharge cut-off voltage of 0.4 V was applied to acquire a better cycle stability, obtaining a higher reversible capacity 154 mA h g⁻¹, corresponding to a capacity retention of 35% (0.325% decay per cycle), whereas the capacity was depressed to 440 mA h g⁻¹. The cycle stability was further improved as a higher discharge cut-off voltage of 0.6 V was employed, reaching a reversible capacity of 151 mA h g⁻¹ after 200 cycles, in correspondence to a capacity retention of 47.2% (0.264% decay per cycle), accompanied by a reversible capacity of 320 mA h g⁻¹. Motivated by these results, a higher discharge cut-off voltage of 0.8 V was performed. It is obvious that the cycle stability is significantly enhanced and the battery delivered a reversible capacity of 293 mA h g⁻¹; and it could exhibit a reversible capacity of 253 mA h g⁻¹ even after 300 cycles, showing a capacity retention of 86.3% (0.045% decay per cycle). The corresponding charge-discharge profiles are shown in Supplementary Fig. S7.

The rate performance of the CCS cathode was investigated with a discharge cut-off voltage of 0.8 V (Fig. 4d). At a low current density of 100 mA g⁻¹, the battery could exhibit a medium discharge voltage of 1.3 V and a reversible discharge capacity of 343 mA h g⁻¹, corresponding to a high energy density of ~445 Wh Kg⁻¹, which is comparable to other cathode materials of PIBs [4–6,8–11,15,19,50,57–66]. Besides, the battery still could deliver a reversible capacity of 275, 206, 150, 115, and 94 mA h g⁻¹, respectively, even though the higher current densities of 200, 400, 600, 800 and 1000 mA g⁻¹ were applied. Moreover, the capacity could recover to 307 mA h g⁻¹ when the current density returned to 100 mA g⁻¹, and it still could deliver a reversible capacity of 290 mA h g⁻¹ after 100 cycles at various current densities, expressing a superior recovery capability at large current densities. Besides, when a low current density of 70 mA g⁻¹ was applied (Supplementary Fig. S8), the battery could deliver a high reversible capacity of 325 mA h g⁻¹. For comparison purposes, the pure polyacrylonitrile annealed at the same condition was also prepared. Supplementary Fig. S9 exhibits the electrochemical performance of pure polyacrylonitrile annealed at 350 °C, 450 °C and 550 °C. The charge/discharge profiles show that the capacity of the pure polyacrylonitrile was pretty low compared with the CCS, and the main capacity of the pure polyacrylonitrile is below 0.5 V, pointing to that the main capacity of the CCS with the voltage cut-off of 0.8–3.0 V is from the sulfur in the CCS.

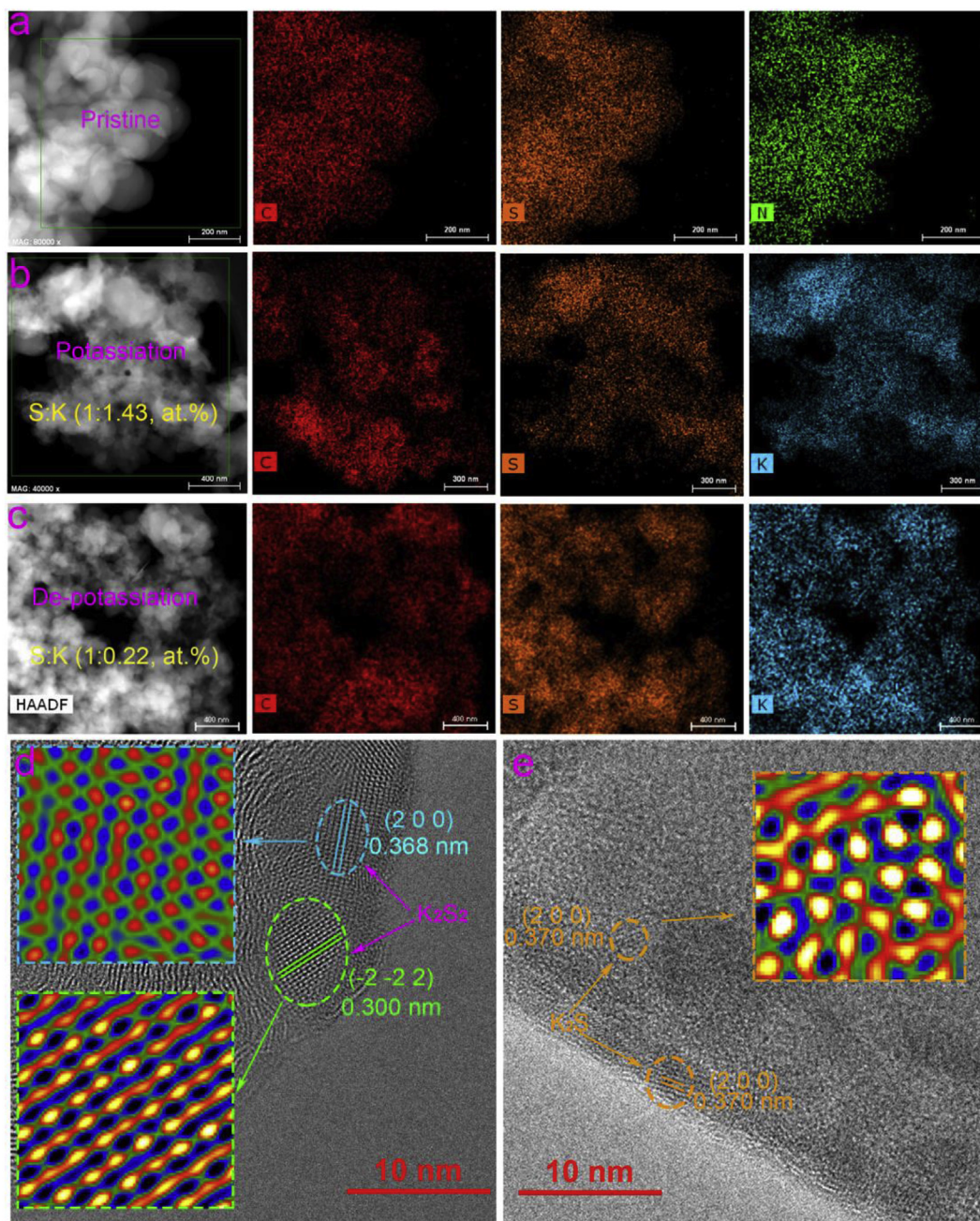


Fig. 3. The TEM elemental mappings of the electrodes at different states during the initial cycle. a) Pristine state. b) Potassiation state (discharged to 0.1 V). c) De-potassiation state (charged to 3.0 V). d) and e) The high-resolution TEM image of the electrode at potassiation state (discharged to 0.1 V).

In order further understand the evolution of S in this system with a discharge voltage cut-off of 0.8 V, ex-situ XRD was conducted during the second cycle (Supplementary Fig. S10). Obviously, the peaks of K_2S_3 , K_2S_5 and K_2S_6 could be found when the battery discharged to 1.6 V; and a new compound of K_2S_4 was presented when the battery discharged to 1.2 V; while K_2S , K_2S_2 and K_2S_3 could be found when the battery discharged to 0.8 V. Nonetheless, peaks of K_2S_3 and K_2S_4 could be observed when the battery charged to 1.8 V; and new compound of K_2S_6 could be found when the battery charged to 2.4 V; finally, only two compounds of K_2S_5 and K_2S_6 could be observed when the battery charged to 3.0 V. The ex-situ XRD demonstrated that the evolution of S in the electrode: the long-chain polysulfides will be accept K^+ and formation

of short-chain sulfides during discharge process; to the contrary, the short-chain sulfides will become long-chain polysulfides during charge process.

Furthermore, the morphology evolution was investigated to understand the structure stability of the CCS with various cut-off voltages. With the discharge cut-off voltage of 0.8 V (Fig. 4e), the morphology of CCS remained intact after 10 cycles, and it still maintained, to a great extent, even after 50 cycles. The stable structure might be responsible for the superior cycle stability with the cut-off voltage range of 3.0–0.8 V. However, CCS was gradually pulverized during cycling with a lower discharge cut-off voltage of 0.1 V (Fig. 4f), indicating that an excessive amount of K^+ reacting with the CCS will result in a huge volume expansion and give rise to

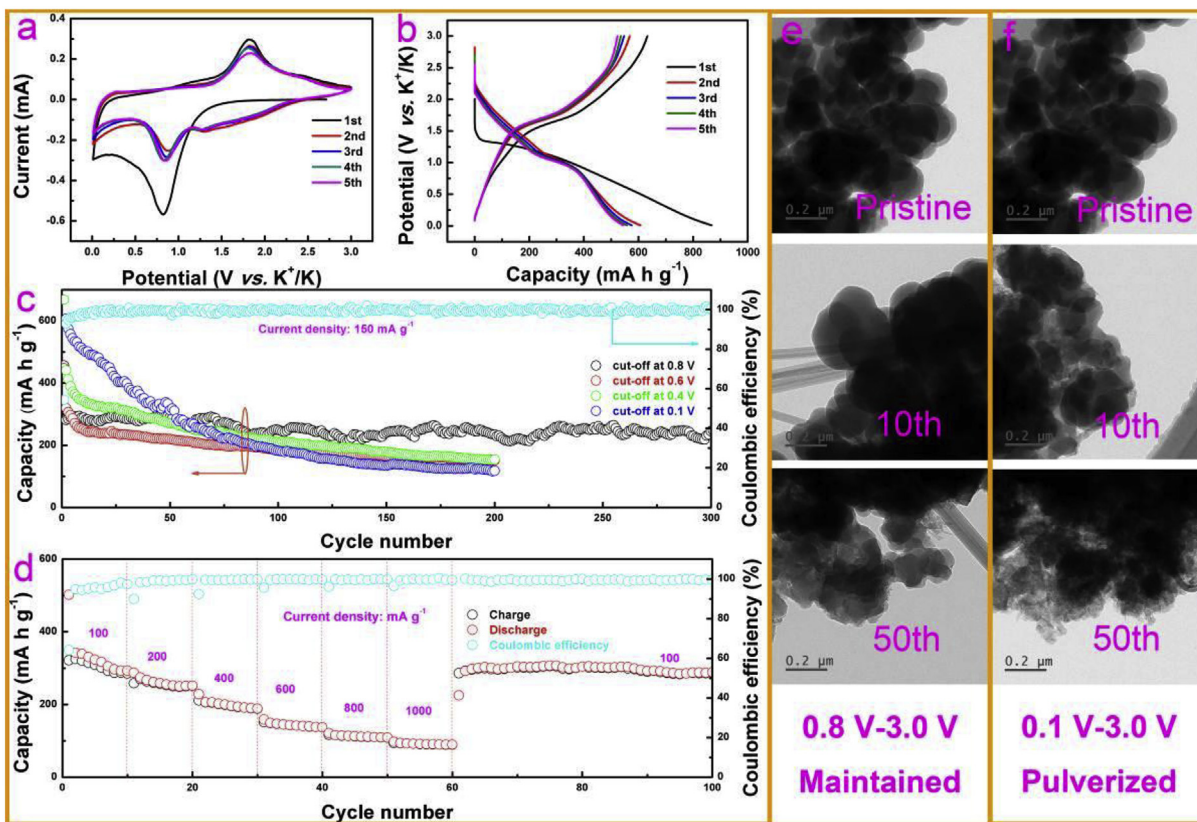


Fig. 4. The electrochemical performance and morphology evolution of the cathode. a) CV curves with a scan rate of 0.2 mV s^{-1} . b) The typical charge/discharge profiles at 150 mA g^{-1} . c) Cycle stability of CCS electrode with different discharge cut-off voltage. d) Rate performance of the CCS electrode with discharge cut-off voltage of 0.8 V . The TEM images of the electrodes at different cycles (morphology evolution) with discharge cut-off voltage of e) 0.8 V and f) 0.1 V .

the structure pulverization and rapid capacity decay. Therefore, a sufficient volume space is required in designing electrode materials for KIBs in order to accommodate the large volume expansion during potassiation process. The excellent electrochemical performance of the CCS for K-S batteries is due to not only the covalent and confined sulfur in the CCS but also the well maintained morphology of CCS.

4. Conclusion

A room temperature potassium-sulfur battery was successfully developed. No shuttle effect was observed in the K-S batteries benefiting from the covalent and confined sulfur in the CCS as well as the carbonate electrolyte. As a result, with a voltage range of $0.8\text{--}3.0 \text{ V}$, the K-S battery could deliver a high energy density of $\sim 445 \text{ Wh Kg}^{-1}$, a high Coulombic efficiency around 100%, and a superior cycle stability with a capacity retention of 86.3% over 300 cycles. This work displayed the basic study on rechargeable potassium-sulfur batteries and may provide a guidance for designing sulfur based electrode materials for potassium based ion batteries.

Acknowledgements

This work was financially supported by National Natural Science Foundation of China (Nos. 51672078 and 21473052) and Hunan University State Key Laboratory of Advanced Design and Manufacturing for Vehicle Body Independent Research Project (No. 71675004), Hunan Youth Talents (2016RS3025), and Foundation of State Key Laboratory of Coal Conversion (Grant No. J17-18-903).

“Author 1 and Author 2 contributed equally to this work.”

Appendix A. Supplementary data

Supplementary data to this article can be found online at <https://doi.org/10.1016/j.electacta.2018.10.040>.

References

- [1] W. Luo, F. Shen, C. Bommier, H. Zhu, X. Ji, L. Hu, Na-ion battery anodes: materials and electrochemistry, *Acc. Chem. Res.* 49 (2016) 231–240.
- [2] W. Luo, J. Wan, B. Ozdemir, W. Bao, Y. Chen, J. Dai, H. Lin, Y. Xu, F. Gu, V. Barone, L. Hu, Potassium ion batteries with graphitic materials, *Nano Lett.* 15 (2015) 7671–7677.
- [3] D. Su, A. McDonagh, S.Z. Qiao, G. Wang, High-capacity aqueous potassium-ion batteries for large-scale energy storage, *Adv. Mater.* 29 (2017), 1604007.
- [4] X. Wang, X. Xu, C. Niu, J. Meng, M. Huang, X. Liu, Z. Liu, L. Mai, Earth abundant Fe/Mn-based layered oxide interconnected nanowires for advanced K-ion full batteries, *Nano Lett.* 17 (2017) 544–550.
- [5] L. Xue, Y. Li, H. Gao, W. Zhou, X. Lu, W. Kaveevivitchai, A. Manthiram, J.B. Goodenough, Low-cost high-energy potassium cathode, *J. Am. Chem. Soc.* 139 (2017) 2164–2167.
- [6] C.L. Zhang, Y. Xu, M. Zhou, L.Y. Liang, H.S. Dong, M.H. Wu, Y. Yang, Y. Lei, Potassium prussian blue nanoparticles: a low-cost cathode material for potassium-ion batteries, *Adv. Funct. Mater.* 27 (2017), 1604307.
- [7] W. Zhang, J. Mao, S. Li, Z. Chen, Z. Guo, Phosphorus-based alloy materials for advanced potassium-ion battery anode, *J. Am. Chem. Soc.* 139 (2017) 3316–3319.
- [8] Y.H. Zhu, Y.B. Yin, X. Yang, T. Sun, S. Wang, Y.S. Jiang, J.M. Yan, X.B. Zhang, Transformation of rusty stainless-steel meshes into stable, low-cost, and binder-free cathodes for high-performance potassium-ion batteries, *Angew. Chem. Int. Ed.* 56 (2017) 7881–7885.
- [9] A. Eftekhari, Potassium secondary cell based on Prussian blue cathode, *J. Power Sources* 126 (2004) 221–228.
- [10] C.D. Wessells, S.V. Peddada, R.A. Huggins, Y. Cui, Nickel hexacyanoferrate nanoparticle electrodes for aqueous sodium and potassium ion batteries,

- Nano Lett. 11 (2011) 5421–5425.
- [11] Y.N. Chen, W. Luo, M. Carter, L.H. Zhou, J.Q. Dai, K. Fu, S. Lacey, T. Li, J.Y. Wan, X.G. Han, Y.P. Bao, L.B. Hu, Organic electrode for non-aqueous potassium-ion batteries, *Nano Energy* 18 (2015) 205–211.
- [12] A. Eftekhari, Z. Jian, X. Ji, Potassium secondary batteries, *ACS Appl. Mater. Interfaces* 9 (2017) 4404–4419.
- [13] C. Chen, Z. Wang, B. Zhang, L. Miao, J. Cai, L. Peng, Y. Huang, J. Jiang, Y. Huang, L. Zhang, J. Xie, Nitrogen-rich hard carbon as a highly durable anode for high-power potassium-ion batteries, *Energy Storage Mater.* 8 (2017) 161–168.
- [14] Z.L. Jian, S. Hwang, Z.F. Li, A.S. Hernandez, X.F. Wang, Z.Y. Xing, D. Su, X.L. Ji, Hard-soft composite carbon as a long-cycling and high-rate anode for potassium-ion batteries, *Adv. Funct. Mater.* 27 (2017), 1700324.
- [15] Y.J. Liu, Z.X. Tai, Q. Zhang, H.Q. Wang, W.K. Pang, H.K. Liu, K. Konstantinov, Z.P. Guo, A new energy storage system: rechargeable potassium-selenium battery, *Nano Energy* 35 (2017) 36–43.
- [16] J.C. Pramudita, D. Sehwat, D. Goonetilleke, N. Sharma, An initial review of the status of electrode materials for potassium-ion batteries, *Adv. Energy Mater.* 7 (2017) 1602911.
- [17] H. Gao, T.F. Zhou, Y. Zheng, Q. Zhang, Y.Q. Liu, J. Chen, H.K. Liu, Z.P. Guo, CoS quantum dot nanoclusters for high-energy potassium-ion batteries, *Adv. Funct. Mater.* 27 (2017), 1702634.
- [18] S.K. Chong, Y.Z. Chen, Y. Zheng, Q. Tan, C.Y. Shu, Y.N. Liu, Z.P. Guo, Potassium ferrocyanide nanoparticles as a high capacity and ultralong life cathode material for nonaqueous potassium-ion batteries, *J. Mater. Chem. A* 5 (2017) 22465–22471.
- [19] G. He, L.F. Nazar, Crystallite size control of prussian white analogues for nonaqueous potassium-ion batteries, *ACS Energy Lett.* 2 (2017) 1122–1127.
- [20] Z. Xing, Z. Jian, W. Luo, Y. Qi, C. Bommier, E.S. Chong, Z. Li, L. Hu, X. Ji, A perylene anhydride crystal as a reversible electrode for K-ion batteries, *Energy Storage Mater.* 2 (2016) 63–68.
- [21] K. Share, A.P. Cohn, R. Carter, B. Rogers, C.L. Pint, Role of nitrogen doped graphene for improved high capacity potassium ion battery anodes, *ACS Nano* 10 (2016) 9738–9744.
- [22] Y. Dong, Z.S. Wu, S. Zheng, X. Wang, J. Qin, S. Wang, X. Shi, X. Bao, Ti₃C₂ MXene-derived sodium/potassium titanate nanoribbons for high-performance sodium/potassium ion batteries with enhanced capacities, *ACS Nano* 11 (2017) 4792–4800.
- [23] J. Zhao, X. Zou, Y. Zhu, Y. Xu, C. Wang, Electrochemical intercalation of potassium into graphite, *Adv. Funct. Mater.* 26 (2016) 8103–8110.
- [24] T. Deng, X. Fan, C. Luo, J. Chen, L. Chen, S. Hou, N. Eidson, X. Zhou, C. Wang, Self-templated formation of P2-type K_{0.6}CoO₂ microspheres for high reversible potassium-ion batteries, *Nano Lett.* 18 (2018) 1522–1529.
- [25] L. Fan, K. Lin, J. Wang, R. Ma, B. Lu, A nonaqueous potassium-based battery-supercapacitor hybrid device, *Adv. Mater.* 30 (2018) 1800804.
- [26] L. Fan, S. Chen, R. Ma, J. Wang, L. Wang, Q. Zhang, E. Zhang, Z. Liu, B. Lu, Ultrastable potassium storage performance realized by highly effective solid electrolyte interphase layer, *Small* 14 (2018) 1801806.
- [27] J. Ge, L. Fan, J. Wang, Q. Zhang, Z. Liu, E. Zhang, Q. Liu, X. Yu, B. Lu, MoSe₂/N-Doped carbon as anodes for potassium-ion batteries, *Adv. Energy Mater.* (2018), 1801477.
- [28] X. Han, Y. Liu, Z. Jia, Y.C. Chen, J. Wan, N. Weadock, K.J. Gaskell, T. Li, L. Hu, Atomic-layer-deposition oxide nanogluue for sodium ion batteries, *Nano Lett.* 14 (2014) 139–147.
- [29] Y. Wen, K. He, Y. Zhu, F. Han, Y. Xu, I. Matsuda, Y. Ishii, J. Cumings, C. Wang, Expanded graphite as superior anode for sodium-ion batteries, *Nat. Commun.* 5 (2014) 4033.
- [30] W. Luo, Z. Jian, Z. Xing, W. Wang, C. Bommier, M.M. Lerner, X. Ji, Electrochemically expandable soft carbon as anodes for Na-ion batteries, *ACS Cent. Sci.* 1 (2015) 516–522.
- [31] L. Fan, B. Lu, Reactive oxygen-doped 3D interdigital carbonaceous materials for Li and Na ion batteries, *Small* 12 (2016) 2783–2791.
- [32] L. Fan, Q. Liu, S.H. Chen, Z. Xu, B.G. Lu, Soft carbon as anode for high-performance sodium-based dual ion full battery, *Adv. Energy Mater.* 7 (2017), 1602778.
- [33] Y. Xiao, S.H. Lee, Y.K. Sun, The application of metal sulfides in sodium ion batteries, *Adv. Energy Mater.* 7 (2017), 1601329.
- [34] Z.H. Zhang, Z.L. Cui, L.X. Qiao, J. Guan, H.M. Xu, X.G. Wang, P. Hu, H.P. Du, S.Z. Li, X.H. Zhou, S.M. Dong, Z.H. Liu, G.L. Cui, L.Q. Chen, Novel Design concepts of efficient Mg-ion electrolytes toward high-performance magnesium-selenium and magnesium-sulfur batteries, *Adv. Energy Mater.* 7 (2017), 1602055.
- [35] M.C. Lin, M. Gong, B. Lu, Y. Wu, D.Y. Wang, M. Guan, M. Angell, C. Chen, J. Yang, B.J. Hwang, H. Dai, An ultrafast rechargeable aluminium-ion battery, *Nature* 520 (2015) 325–328.
- [36] A. Manthiram, X. Yu, Ambient temperature sodium-sulfur batteries, *Small* 11 (2015) 2108–2114.
- [37] X.W. Yu, Z.H. Bi, F. Zhao, A. Manthiram, Polysulfide-shuttle control in lithium-sulfur batteries with a chemically/electrochemically compatible NaSICON-type solid electrolyte, *Adv. Energy Mater.* 6 (2016), 1601392.
- [38] L. Luo, A. Manthiram, Rational Design of high-loading sulfur cathodes with a poached-egg-shaped architecture for long-cycle lithium-sulfur batteries, *ACS Energy Lett.* 2 (2017) 2205–2211.
- [39] X. Yu, A. Manthiram, Electrode-electrolyte interfaces in lithium-sulfur batteries with liquid or inorganic solid electrolytes, *Acc. Chem. Res.* 50 (2017) 2653–2660.
- [40] L. Fan, R.F. Ma, Y.H. Yang, S.H. Chen, B.A. Lu, Covalent sulfur for advanced room temperature sodium-sulfur batteries, *Nano Energy* 28 (2016) 304–310.
- [41] X. Liang, Y. Rangom, C.Y. Kwok, Q. Pang, L.F. Nazar, Interwoven MXene nanosheet/carbon-nanotube composites as Li-S cathode hosts, *Adv. Mater.* 29 (2017) 1603040.
- [42] Q. Pang, X. Liang, C.Y. Kwok, J. Kulisch, L.F. Nazar, A comprehensive approach toward stable lithium-sulfur batteries with high volumetric energy density, *Adv. Energy Mater.* 7 (2017) 1601630.
- [43] W. Chen, T. Qian, J. Xiong, N. Xu, X. Liu, J. Liu, J. Zhou, X. Shen, T. Yang, Y. Chen, C. Yan, A new type of multifunctional polar binder: toward practical application of high energy lithium sulfur batteries, *Adv. Mater.* 29 (2017), 1605160.
- [44] N. Xu, T. Qian, X. Liu, J. Liu, Y. Chen, C. Yan, Greatly suppressed shuttle effect for improved lithium sulfur battery performance through short chain intermediates, *Nano Lett.* 17 (2017) 538–543.
- [45] T. Zhou, Y. Zhao, G. Zhou, W. Lv, P. Sun, F. Kang, B. Li, Q.H. Yang, An in-plane heterostructure of graphene and titanium carbide for efficient polysulfide confinement, *Nano Energy* 39 (2017) 291–296.
- [46] H. Shi, W. Lv, C. Zhang, D. Wang, G. Ling, Y. He, F. Kang, Q. Yang, Functional carbons remedy the shuttling of polysulfides in lithium-sulfur batteries: confining, trapping, blocking, and breaking up, *Adv. Funct. Mater.* 28 (2018) 1800508.
- [47] D. Liu, C. Zhang, G. Zhou, W. Lv, G. Ling, L. Zhi, Q.H. Yang, Catalytic effects in lithium-sulfur batteries: promoted sulfur transformation and reduced shuttle effect, *Adv. Sci.* 5 (2018), 1700270.
- [48] J. Wang, J. Yang, C. Wan, K. Du, J. Xie, N. Xu, Sulfur composite cathode materials for rechargeable lithium batteries, *Adv. Funct. Mater.* 13 (2003) 487–492.
- [49] L. Fan, S. Chen, J. Zhu, R. Ma, S. Li, R. Podila, A.M. Rao, G. Yang, C. Wang, Q. Liu, Z. Xu, L. Yuan, Y. Huang, B. Lu, Simultaneous suppression of the dendrite formation and shuttle effect in a lithium-sulfur battery by bilateral solid electrolyte interface, *Adv. Sci.* 5 (2018) 1700934.
- [50] Q. Zhao, Y. Hu, K. Zhang, J. Chen, Potassium-sulfur batteries: a new member of room-temperature rechargeable metal-sulfur batteries, *Inorg. Chem.* 53 (2014) 9000–9005.
- [51] X. Lu, M.E. Bowden, V.L. Sprenkle, J. Liu, A low cost, high energy density, and long cycle life potassium-sulfur battery for grid-scale energy storage, *Adv. Mater.* 27 (2015) 5915–5922.
- [52] J.Y. Hwang, H.M. Kim, C.S. Yoon, Y.K. Sun, Toward high-safety potassium-sulfur batteries using a potassium polysulfide catholyte and metal-free anode, *ACS Energy Lett.* (2018) 540–541.
- [53] Y. Xu, Y. Wen, Y. Zhu, K. Gaskell, K.A. Cychosz, B. Eichhorn, K. Xu, C. Wang, Confined sulfur in microporous carbon renders superior cycling stability in Li/S batteries, *Adv. Funct. Mater.* 25 (2015) 4312–4320.
- [54] L. Sun, M. Li, Y. Jiang, W. Kong, K. Jiang, J. Wang, S. Fan, Sulfur nanocrystals confined in carbon nanotube network as a binder-free electrode for high-performance lithium sulfur batteries, *Nano Lett.* 14 (2014) 4044–4049.
- [55] S. Wei, L. Ma, K.E. Hendrickson, Z. Tu, L.A. Archer, Metal-sulfur battery cathodes based on PAN-sulfur composites, *J. Am. Chem. Soc.* 137 (2015) 12143–12152.
- [56] G.J. Janz, J.R. Downey Jr., E. Roduner, Raman studies of sulfur-containing anions in inorganic polysulfides. Potassium polysulfides, *Inorg. Chem.* 15 (1976) 1755–1759.
- [57] P. Padigi, J. Thiebes, M. Swan, G. Goncher, D. Evans, R. Solanki, Prussian green: a high rate capacity cathode for potassium ion batteries, *Electrochim. Acta* 166 (2015) 32–39.
- [58] J. Han, Y. Niu, S.J. Bao, Y.N. Yu, S.Y. Lu, M. Xu, Nanocubic KTi₂(PO₄)₃ electrodes for potassium-ion batteries, *Chem. Commun.* 52 (2016) 11661–11664.
- [59] Z.L. Jian, Y.L. Liang, I.A. Rodriguez-Perez, Y. Yao, X.L. Ji, Poly(anthraquinonyl sulfide) cathode for potassium-ion batteries, *Electrochem. Commun.* 71 (2016) 5–8.
- [60] C. Vaalma, G.A. Giffin, D. Buchholz, S. Passerini, Non-Aqueous K-ion battery based on layered K_{0.3}MnO₂ and hard carbon/carbon black, *J. Electrochem. Soc.* 163 (2016) A1295–A1299.
- [61] X.F. Bie, K. Kubota, T. Hosaka, K. Chihara, S. Komaba, A novel K-ion battery: hexacyanoferrate(II)/graphite cell, *J. Mater. Chem. A* 5 (2017) 4325–4330.
- [62] K. Chihara, A. Katogi, K. Kubota, S. Komaba, KVPO₄F and KVOPO₄ toward 4 volt-class potassium-ion batteries, *Chem. Commun.* 53 (2017) 5208–5211.
- [63] L. Fan, Q. Liu, S. Chen, K. Lin, Z. Xu, B. Lu, Potassium-based dual ion battery with dual-graphite electrode, *Small* 13 (2017), 1701011.
- [64] L. Fan, Q. Liu, Z. Xu, B.G. Lu, An organic cathode for potassium dual-ion full battery, *ACS Energy Lett.* 2 (2017) 1614–1620.
- [65] J. Han, G.N. Li, F. Liu, M. Wang, Y. Zhang, L. Hu, C. Dai, M. Xu, Investigation of K₃V₂(PO₄)₃/C nanocomposites as high-potential cathode materials for potassium-ion batteries, *Chem. Commun.* 53 (2017) 1805–1808.
- [66] Y. Hironaka, K. Kubota, S. Komaba, P₂- and P₃-K_xCoO₂ as an electrochemical potassium intercalation host, *Chem. Commun.* 53 (2017) 3693–3696.